Diss. 2005 - 10
August

First Direct Observation of Bound-State Beta-Decay: Measurements of Branching and Lifetime of $^{207}Tl^{81+}$ Fragments

David Boutin

(Dissertation Justus-Liebig Universität / Gießen)

Gesellschaft für Schwerionenforschung mbH
Planckstraße 1 · D-64291 Darmstadt · Germany
Postfach 11 05 52 · D-64220 Darmstadt · Germany

Inaugural Dissertation zur Erlangung des
Doktorgrades der Naturwissenschaften
der Justus-Liebig Universität Gießen
(Fachbereich Physik)

First Direct Observation of Bound-State Beta-Decay: Measurements of Branching and Lifetime of $^{207}Tl^{81+}$ Fragments

vorgelegt von
David Boutin
geboren in Nantes
Juli 2005

Gutachter: Prof Dr. Hans Geissel
Prof Dr. Volker Metag
Prof Dr. Werner Scheid

... et Pangloss disait quelquefois à Candide : "Tous les événements sont enchaînés dans le meilleur des mondes possibles : car enfin si vous n'aviez pas été chassé d'un beau château à grands coups de pied dans le derrière pour l'amour de mademoiselle Cunégonde, si vous n'aviez pas été mis à l'Inquisition, si vous n'aviez pas couru l'Amérique à pied, si vous n'aviez pas donné un bon coup d'épée au baron, si vous n'aviez pas perdu tous vos moutons du bon pays d'Eldorado, vous ne mangeriez pas ici des cédrats confits et des pistaches. - Cela est bien dit, répondit Candide, mais il faut cultiver notre jardin."

Voltaire, Candide

Zusammenfassung

Der β-Zerfall in gebundene Endzustände des freigesetzten Elektrons ist ein seit vielen Jahrzehnten vorhergesagter aber erst vor wenigen Jahren bei GSI erstmalig experimentell nachgewiesener Zerfallsprozeß der schwachen Wechselwirkung. Während er in Atomen und niedrig geladenen Ionen vernachlässigbar ist, kann er die Zerfallseigenschaften in hochgeladenen Ionen und vollständig ionisierten Kernen dramatisch beeinflussen. Als Beispiel ist der Zerfall von ^{163}Dy zu nennen , welches unter Normalbedingungen einen negativen β-Zerfalls Q-Wert besitzt und folglich *stabil* ist, aber bei vollständiger Ionisierung einen positiven Q-Wert erhält und *instabil* wird. Auch der Zerfall von hochgradig ionisiertem ^{187}Re, welchem astrophysikalische Bedeutung bei der Altersbestimmung des Universums zukommt , wird vom gebundenen β-Zerfall dominiert und die Halbwertszeit des neutralen Atoms sinkt von 41,2(2) Mrd. Jahren um neun Größenordnungen auf 33(2) Jahre im vollständig ionisierten Kern. Während diese Pionier-Experimente auf den (indirekten) Nachweis an sich bzw. auf Halbwertszeitmessungen ausgerichtet waren, waren die Ziele der vorliegenden Arbeit die erstmalige *direkte* Beobachtung des gebundenen β-Zerfalls sowie die erstmalige Messung eines Verzweigungsverhältnisses des β-Zerfalls ins Kontinuum (λ_c) und in gebundene Zustände (λ_b). Dieses Verzweigungsverhältnis, welches für die zeitumgekehrten Prozesse des Elektroneneinfangs und des β^+-Zerfalls theoretisch und experimentell im Detail untersucht und verstanden ist, ist für den β^--Zerfall bisher nur theoretisch bekannt, so daß die vorliegenden Ergebnisse einen wichtigen Test der Fermi'schen Theorie der schwachen Wechselwirkung darstellen.
Für das Experiment wurde das Nuklid ^{207}Tl ausgewählt, welches einerseits eine genügend hohe Ordnungszahl und einen hinreichend kleinen Q-Wert von etwa 1,4 MeV besitzt, so daß im Hinblick auf die Meßgenauigkeit ein genügend großes Verzweigungsverhältnis erreicht wird (die theoretische Vorhersage beträgt in diesem Fall $\lambda_b/\lambda_c = 0,171(1)$), andererseits ist der Q-Wert groß genug, so daß mit der verwendeten zeitaufgel"osten Schottky-Spektroskopie eine *gleichzeitige* Beobachtung der "Mutter"- (vollständig ionisierte ^{207}Tl^{81+}-Kerne) und "Tochter" nuklide (H-ähnliche ^{207}Pb^{81+}-Ionen), was für die *direkte* Beobachtung essentiell ist, gewährleistet wird, und auch die Halbwertszeit liegt mit etwa vier Minuten in einer hinsichtlich der eingesetzten Experimentiertechnik idealen Größenordnung. Zunächst wurde in einem Pilotexperiment die prinzipielle Durchführbarkeit untersucht. Dabei stellte sich heraus, daß die Kühlkraft der Elektronenkühlung im Experimentierspeicherring ESR nicht ausreicht um die vom Fragmentseparators FRS gelieferten Fragmentstrahlen, die relative Impulsbreiten im Prozentbereich aufweisen, schnell genug kühlen zu können. Daher wurde im Hauptexperiment erstmals die stochastische Kühlung für Sekundärstrahlen am ESR eingesetzt. Dazu wurde ^{207}Tl durch die Fragmentationsreaktion eines ^{208}Pb-Strahls in einem Beryllium-Target am Eingang des FRS erzeugt, mittels der $B\rho-\Delta E-B\rho$–Methode isotopenrein separiert und in den ESR eingeschossen. Durch die Kombination von stochastischer und Elektronenkühlung wurden jetzt Kühlzeiten von etwa sechs bis sieben Sekunden erzielt. Dadurch kann der Bereich des schnellen Anstieg der Intensität der H-ähnlichen ^{207}Pb^{81+}-Ionen, auf welchen die Bestimmung des Verzweigungsverhältnisses sehr sensitiv ist, gut beobachtet werden.

Ferner kann aufgrund der kurzen Kühl- und Meßzeiten auch der isomere Zustand ^{207m}Tl untersucht werden.
Die Auswertung der Daten liefert folgende Ergebnisse. Die beobachtete Halbwertszeit des $^{207}Tl^{81+}$ liegt mit $T_{1/2} = 255(17)$ s etwa 12 % unter der des neutralen Atoms. Zwar spielen hier auch Effekte wie die fehlende Abschirmung durch die fehlende Elektronenhülle sowie die Modifikation des Q-Werts eine Rolle, der hauptsächliche Effekt aber kommt von dem nun zusätzlich verfügbaren Phasenraum, der zum neu hinzukommenden Zerfallskanal des gebundenen β-Zerfalls führt. Dessen partielle Halbwertszeit von $T_{1/2}(\beta_b) = 1582(150)$ s liefert zusammen mit der Halbwertszeit des Kontinuumszerfalls von $T_{1/2}(\beta_c) = 304(18)$ s das gesuchte Verzweigungsverhältnis von $\lambda_b/\lambda_c = 0{,}192(20)$, welches in hervorragender Übereinstimmung mit dem theoretisch vorhergesagten Wert ist.
Zusätzlich zu den genannten Ergebnissen befindet sich auch der für die Halbwertszeit des nackten isomeren Zustands gemessene Wert von $1,47(32)$ s in Übereinstimmung mit dem erwarteten Wert. Auch hierbei weicht die Halbwertszeit von der des neutralen Atoms ab $1,33(11)$ s, da aufgrund der fehlenden Elektronenhülle die Möglichkeit der Konversion nicht mehr gegeben ist, was zu einer größeren Lebensdauer führt.
Schließlich erlaubt die zeitaufgelöste Schottky-Spektroskopie das Studium der Bevölkerungswahrscheinlichkeit isomerer Zustände in Fragmentationsreaktionen. Zusammen mit Literaturwerten werden die hier gewonnenen Daten mit einem einfachen Modell verglichen.

Summary

It has been predicted since several decades that the change in the number of electrons bound to a particular nuclide could lead to a drastic modification of the decay properties of this nuclide. In the particular case of β^- decay, the decay "constant" of a nuclide could be modified, due to the apparation of a "new" decay mode, the bound-state β-decay. It is favoured in the case of highly-ionized atoms, and can have a influence of astrophysical nucleosynthesis, in particular in the s-process.

This decay mode could be observed in pioneering experiments, due to the possibility to accumulate and store highly-charged ions for a long period of time. The first experimental observation of bound-state β-decay showed, that due solely to the electron stripping, a *stable* nuclide, e.g. ^{163}Dy, became *unstable*. Also a drastic modification of the half-life of bare ^{187}Re, from $4.12(2) \times 10^{10}$ years down to 32.9(20) years, could be observed. It was mainly due to the possibility for the mother nuclide to decay into a previously unaccessible nuclear level of the daughter nuclide. In these experiments nuclides where bound-state β-decay was the only energetically possible decay mode have been studied. It was proposed to study a nuclide where this decay mode was competing with continuum-state β-decay, in order to measure their respective branchings. The ratio β_b/β_c could also be evaluated for the first time, in contrary to the ratio EC/β^+ which had already experimental information.

^{207}Tl was chosen due to its high atomic number, and Q-value about 1.4 MeV, small enough to enhance the β_b probability (theoretical predictions give $\beta_b/\beta_c = 0.171(1)$), and large enough to allow the use of time-resolved Schottky Mass Spectrometry (SMS) to study the evolution of mother and bound-state β-decay daughter ions. The neutral half-life of about 5 min is ideal to study the decay of this nuclide.

The decay properties of the ground state and isomeric state of ^{207}Tl^{81+} have been investigated at the GSI accelerator facility in two separate experiments. These ions have been produced by the projectile fragmentation of ^{208}Pb in a 4 g/cm^2 Be target. The fragments were separated from contaminants by the in-flight fragment separator FRS. They were injected into the storage ring ESR and cooled. The electron cooling system reduced the momentum distribution of the ions down to 5×10^{-7}. But problems with the cooling time and efficiency lead to a second experiment. This time in addition to the electron cooling the stochastic precooling was applied, *for the first time* for fragments. It reduced the overall cooling time down to 6-7 s. The data obtained was analyzed via time-resolved Schottky Mass Spectrometry (SMS). For the first time β-decay where the electron could go either to a bound state (atomic orbitals) and lead to ^{207}Pb^{81+} as a daughter nuclide, or to a continuum state and lead to ^{207}Pb^{82+}, has been observed. The respective branchings of these two processes could be measured as well. The deduced total nuclear half-life of 255(17) s for ^{207}Tl^{81+}, was slightly modified with respect to the half-life of the neutral atom of 286(2) s. It was nevertheless in very good agreement with calculations based on the assumption that the β-decay was following an allowed type of transition. The branching $\beta_b/\beta_c = 0.192(20)$, was also in very good agreement with the same calculations.

The application of stochastic precooling allowed to observe in addition the 1348 keV short-lived isomeric state of ^{207}Tl. The half-life of this isomeric state was measured as 1.47(32) s, which shows a small deviation compared to the half-life for the neutral atom, as 1.33(11) s. This difference was explained by the blocking of the internal conversion channel in the isomeric decay, due to the absence of bound electrons. From the extrapolated ratio of the $^{207}Tl^{81+}$ particles injected into the ESR in the isomeric state to the sum of all $^{207}Tl^{81+}$ particles injected, the isomeric production ratio of ^{207}Tl from the fragmentation process could be evaluated as 0.15(4), which was in good agreement with calculations based on the abrasion-ablation model, deriving a value for the isomeric production ratio of 0.11.

Contents

Chapter 1

Introduction

1.1 Modification of nuclear decay properties of atoms

The natural radioactivity, discovered by Becquerel in 1895, has been subsequently subdivided into three main components, distinguished by the emitted particle, and called α, β and γ radioactivity. Only these decay modes will be described in the following. From that period, attempts to modify the decay properties of radioactive nuclides by all possible means (temperature, pressure, electromagnetic fields, ...) have been made. In all cases the relative changes in the lifetimes of the atoms were not observed to be larger than a few 10^{-3} [1, 2, 3]. Therefore, the decay rates or lifetimes, were taken as an invariant property of any nucleon configuration, and appear as a "constant" for any nuclide in the nuclear data tables [4]. Yet it has been predicted that the change in the number of electrons belonging to the atomic cloud surrounding the nucleus can have a strong influence on the decay rate of this nucleus (see ref. [5] for an overview).

In the case of α-decay, the emitted particle is $^4He^{2+}$, thus the emission probability is expected to be modified by the removal of bound electrons, and it has been shown by V. A. Erma [6] that the vanishing of the electron screening, enhancing the Coulomb barrier, can increase the lifetime of fully-ionized atoms up to 50 % (see also [7]). The change of lifetime will be more drastic as the released energy by the decay E_α will be smaller, or as the lifetime will be higher.

For the γ-emitters (isomeric states), the decay process is shared by photon-emission (γ rays) and internal conversion (IC), e.g. the excitation energy of the nucleus is given to a bound electron, thus being excited or emitted. If all bound electrons are removed, obviously the latter process cannot occur, and the lifetime of the state will be increased. Some dramatic changes have been already observed [8, 9] up to factor 30 compared with neutral atoms. One example of the lifetime measurement of an isomeric state is described in chapter 5.

R. Daudel *et al.* [10] pointed out that the removal of bound electrons of any radioactive atom would lead to dramatic changes in lifetimes of β-unstable nuclides. The first two effects resulting from the change of bound electrons are a change in the Q-value of the decay reaction (from the difference in the electron binding energies in mother and daughter nuclides) and in the screening affecting the emitted particles. The third is the appearance of a additional decay channel, the *bound-state β-decay*. An overview of the β-decay theory will be described in

the following sections.

1.2 β-decay theory overview

1.2.1 A brief history

The β radioactivity was discovered as one component of the natural radioactivity (with α and γ components) in the turn of the 20^{th} century. The first experimental observations of this process were electrons emitted from radioactive sources. Further studies [11] showed that the electron energy spectrum was continuous, and that β-decay seemed to violate conservation laws of nuclear physics (in particular energy, spin and parity). The experimental observations convinced W. Pauli in 1930 to propose the emission of a second particle simultaneously with the electron, with negligible mass, no electrical charge, spin 1/2 and positive parity. This particle was called later the *neutrino*, and its experimental evidence was achieved in 1956 [12]. The research on the evaluation of the neutrino mass is still a burning topic in modern physics. Also β-decay where the emitted particle, similar to the electron, had a positive charge (hence called positron) was observed, making the need for a separation between two distinct β-decay modes:

- β^- if the observed charged particle is an electron. It happens to neutron-rich nuclides (compared with stable isotopes)
- β^+ if the observed charged particle is a positron. It happens to neutron-deficient nuclides (also compared with stable isotopes)

A distinction was made between the *neutrino* produced in β^+ decays and the *anti-neutrino* produced in β^- decays. E. Fermi developed in 1934 a theory of β-decay [13], which is still used as a basis nowadays. Still violation of parity was an open question, according to T. D. Lee and C. N. Yang [14] weak interactions processes like β-decay may not always conserve parity. The evidence was found by C. S. Wu *et al.* in a decisive experiment [15] where the decay of polarized ^{60}Co showed electron emission asymmetry in angle. Recent research focuses on other possible violations of conservation laws, like lepton number in double β-decay [16], or CPT (for Charge Parity Time) invariance.

1.2.2 β-decay processes description

In the nucleon scale, the β-decay can be represented as the following:

$$n \rightarrow p + e^- + \bar{\nu_e}, \tag{1.1}$$

for β^-, and:

$$p \rightarrow n + e^+ + \nu_e, \tag{1.2}$$

for β^+.
As shown in equations 1.1 and 1.2, the β-decay represents the transformation of a proton (p) or neutron (n) to the other type of nucleon, with the emission of two leptons. These reactions, as any process in physics are energetically possible only if the Q-value of the reaction, the difference between the total masses of the final

and initial states, is positive. Experimentally the neutron mass is slightly higher than the proton mass, the others particles having a negligible mass compared to the one of the nucleons, thus only the β^- process is observed in nature for a free nucleon. In the atomic medium, equations 1.1 and 1.2 become:

$$ {}^{A}_{Z}X^{q} \rightarrow {}^{A}_{Z+1}Y^{q+1} + e^- + \bar{\nu}_e, \tag{1.3} $$

for β^-, and:

$$ {}^{A}_{Z}X^{q} \rightarrow {}^{A}_{Z-1}Y^{q-1} + e^+ + \nu_e, \tag{1.4} $$

for β^+.
The β-unstable nuclides will decay to isobars by emitting two leptons into the continuum, and by changing their atomic number Z by ± 1, and charge-state q accordingly. The two latter aspect are important from experimental point of view, because mother and daughter nuclide have different charge-state and atomic number .
Both equations can be energetically allowed, because the mass of the nucleus is not the sum of the masses of the nucleons and electrons constituting it, but it has been found to be smaller [17], the difference being called the binding energy. Also the mass of the atomic cloud is less than the sum of the masses of the electrons, giving additional binding energy to the nuclide. The difference in total binding energy between two neighboring isobars will determine which one of the two β-decay processes is energetically allowed and observed. The spin and parity of the nuclear states involved in the β-decay process play also an important role. They will determine the type of transition corresponding to this decay, either *allowed* transition or *forbidden* transition, and indicate how "fast" the transition is.

1.2.3 Allowed transitions

The notation J^{π} is used in the following, where J is the total spin of a system (particle, nucleus) and π his parity. The selection rules for allowed transitions are:

- Leptons $\rightarrow \vec{L}_l = 0$ (no angular momentum carried by the leptons)
- Nucleus $\rightarrow \pi_i \pi_f = +1$ (no parity change)

Since the two leptons can couple to a total intrinsic spin $\vec{S}_l = 0$ or 1, and upon the condition that they don't carry angular momentum, the nucleus can have only a change of total spin $\Delta\vec{J} = \vec{L}_l + \vec{S}_l = 0, 1$. Two different transition modes occur, depending on the alignment of the two lepton spins. If the two leptons have their spin anti-parallel ($\vec{S}_l = 0$), only $\Delta J = 0$ is possible (singlet state). The corresponding transitions are called *Fermi* transitions or *vector* transitions. If the two leptons have their spin parallel ($\vec{S}_l = 1$), $\Delta J = 0, \pm 1$ are possible (triplet state). These transitions are called *Gamow-Teller* (GT) transition or *axial vector* transition.
Transitions where the spins of the final and initial states are $J_f = J_i = 0$ ($0 \rightarrow 0$) are pure Fermi transitions, since $\vec{S}_l = 1$ states cannot be formed with $J_f = J_i = 0$. On the other hand, transitions with $\Delta J = \pm 1$ are pure GT transitions. Other transitions, with $\Delta J = 0$ and $J_i \neq 0$ are mixture of Fermi and GT transitions. A

special case of Fermi transition occurs when the nucleon involved in the β-decay process does not change any of its quantum numbers. This corresponds to $0^+ \rightarrow 0^+$ transitions, being experimentally observed near the N = Z region. These transitions are called *super-allowed*, and their study is very interesting in the sense that the transition is practically independent of the strong interaction.
The decay rate of any transition can be represented as the following [18]:

$$\frac{d\lambda}{dE} = \frac{2\pi}{\hbar} \left|M_{fi}\right|^2 \frac{dn}{dE}, \tag{1.5}$$

where $\left|M_{fi}\right|^2 = \left|< \Psi_f \left|H_{int}\right| \Psi_i >\right|^2$ is the nuclear matrix element corresponding to this transition, $\frac{dn}{dE}$ is the density of states of the created leptons. Equation 1.5 is also called *Fermi's golden rule*. Since the two leptons are relativistic particles, the relativistic relation $E^2 = p^2c^2 + m^2c^4$ can be applied, as well as its derivative $E\ dE = p\ dp\ c^2$. Using the following relation:

$$\frac{dn}{dE} = \frac{dn_e dn_\nu}{dE_e dE_\nu} = \frac{1}{(2\pi\hbar)^6} \frac{p_e^2 dp_e p_\nu^2 dp_\nu}{dE_e dE_\nu} d\Omega_e d\Omega_\nu, \tag{1.6}$$

equation 1.5 is modified as:

$$d\lambda = \frac{1}{(2\pi)^5 c^6 \hbar^7} \left|M_{fi}\right|^2 \ d\Omega_e d\Omega_\nu \ E_e E_\nu \ \sqrt{E_e^2 - m_e^2 c^4} \ \sqrt{E_\nu^2 - m_\nu^2 c^4} \ dEe. \tag{1.7}$$

If $m_\nu \rightarrow 0$, with $E_e + E_\nu = E$ and the notation of the energy in units of $m_e c^2$, equation 1.7 becomes:

$$d\lambda = \frac{1}{(2\pi)^5 c^6 \hbar^7} \left|M_{fi}\right|^2 \ d\Omega_e d\Omega_\nu \ E_e \ \sqrt{E_e^2 - 1} \ (E - E_e)^2 \ dEe. \tag{1.8}$$

By integrating equation 1.8 over the angles $d\Omega_e$, $d\Omega_\nu$, and the electron energy E_e between 1 (electron rest mass) and E (maximum energy available), one gets:

$$\lambda = \frac{(4\pi)^2}{(2\pi)^5 c^6 \hbar^7} \left|M_{fi}\right|^2 \int_1^E E_e \ \sqrt{E_e^2 - 1} \ (E - E_e)^2 \ dEe. \tag{1.9}$$

The integral term is named *integrated Fermi function* or *statistical rate function*, and noted as $f(Z, E)$. Equation 1.9 applies for the decay of a free particle. In the case of decay of a nucleon into the nuclear medium, the charge of the nucleus will affect the electron emission, this effect must be taken into consideration. This is done by adding a factor F(Z,E) into the integral, which is called *Fermi function*. It represents the ratio between the wave function of an electron emitted from a nucleus with atomic number Z and the wave function of the same electron emitted from the same nucleus having a atomic number Z=0. Thus equation 1.9 becomes:

$$\lambda = \frac{(4\pi)^2}{(2\pi)^5 c^6 \hbar^7} \left|M_{fi}\right|^2 \int_1^E E_e \ \sqrt{E_e^2 - 1} \ (E - E_e)^2 F(Z, E) \ dEe. \tag{1.10}$$

In the case of $E \gg 1$, the statistical rate function can be approximated by $f(Z, E) \approx E^5/30$, thus the decay rate will be proportional to E^5. This strong dependence of the decay rate of a β transition with energy is called *Sargent's rule* [18]. To test equation 1.10 the following quantity:

$$K(E_e) = \sqrt{\frac{dN/dE_e}{F(Z,E)E_e\sqrt{E_e^2-1}}}, \tag{1.11}$$

is plotted against the electron energy E_e. From the previous equations it is clear that $K(E_e)$ is proportional to (E - E_e). Thus the so-called *Kurie* plot will look like a straight line, with a cross at K = 0 when E_e = E. This energy is called the *β-endpoint energy*. This behaviour is assumed for all allowed transitions.
In the equations 1.8 to 1.11 the assumption that $m_\nu \rightarrow 0$ has been used. A non-zero mass for the electron neutrino would influence the shape of the energy spectrum of the electron in the region where the electron gets almost all the kinetic energy available, near the β-endpoint energy. If $m_\nu \neq 0$, the modification of these equations leads to:

$$K(E_e) \propto \sqrt{(E-E_e)\sqrt{(E-E_e)^2 - m_\nu^2 c^4}}. \tag{1.12}$$

In order to estimate with the best accuracy the effect of a finite neutrino mass on the Kurie plot, the ideal case is to look at β transitions with the lowest released energy E possible. One suitable candidate is the tritium (^{3}H), which decays by β^- process to ^{3}He + e^- + $\bar{\nu}_e$, with a maximum kinetic energy available for the electron of 18.6 keV. The upper limit obtained for the anti-neutrino mass from this method was 2.8 eV/c^2 (95 % C. L.) [19]. Other recent results [20] from the Super-Kamiokande detector, not related with β-decay measurements, show evidence for neutrino oscillations, leading to a non-zero electron neutrino mass.
The product of $f(Z,E)$ with the partial half-life $t_{1/2}$ for a given transition is called the *ft value*. Since the half-life is defined as $t_{1/2} = \ln 2/\lambda$, it can be written as:

$$f(Z,E) \cdot t_{1/2} \propto \frac{1}{|M_{fi}|^2}. \tag{1.13}$$

The *ft* value of a given transition is proportional to the inverse of the square of the matrix element involved in this transition. Typical *ft* values vary from 10^3 s to 10^{22} s, therefore the base ten logarithm of this value or *log-ft* is usually given in literature. A range of *log-ft* values is characteristic of the type of transition, being super-allowed, allowed or forbidden.

1.2.4 Forbidden transitions

Forbidden transitions follow at least one of the following selection rules:

- Leptons $\rightarrow \vec{L}_l > 0$, (angular momentum carried by the leptons)

or

- Nucleus $\rightarrow \pi_i\pi_f$ = -1. (change of parity)

The emitted leptons have to carry angular momentum $\vec{L}_l$ if this type of transition occur. Considering the electron and neutrino wave functions as plane waves (Born approximation), they can be written as the following [18]:

$$\Psi_{e,\nu}(\vec{x}) = \frac{e^{i\vec{p}\vec{x}/\hbar}}{\sqrt{V}} \equiv \frac{1}{\sqrt{V}}\left[1 + \frac{i}{\hbar}\vec{p}\vec{x} - \frac{1}{2}\left(\frac{\vec{p}\vec{x}}{\hbar}\right)^2 + ...\right], \tag{1.14}$$

where V is a phase space volume element, $\vec{p}$ and $\vec{x}$ are respectively the momentum and position vectors of the particle. Since $\vec{l} = \vec{x} \times \vec{p}$ the previous equation is an expansion of the lepton wave function to angular momenta. In the case of a particle emitted with momentum on the order of few MeV/c and for a nuclear radius of few fm, the product l = p·x/$\hbar$ is approximately equal to 10^{-2}. Since the matrix element is squared in the determination of the decay constant, each unit of l that has to be carried by the leptons will suppress the decay constant by approximately a factor 10^{-4} compared to the case with $l = 0$. These transitions are therefore called *forbidden*, because they are highly suppressed compared to *allowed* ones.

The degree of forbiddeness of a transition is given by the unit of angular momentum carried by the leptons, first-forbidden if $\vec{L}_l = 1$, second-forbidden if $\vec{L}_l = 2$, etc. In nature most of the forbidden transitions are first-forbidden, but in some rare cases higher order forbidden transitions have been observed, an extreme is the fourth-forbidden β^--decay of ^{115}In, with the log-ft value being 22.7 and half-life $6{\times}10^{14}$ years .

Forbidden transitions are classified into two branches, *unique* and *non-unique*, depending on the changes of spin and parity of the nucleus involved in the β^--decay. For unique transitions it appears that only one matrix element contributes to the transition, whereas in non-unique cases several matrix elements will be participating. So forbidden transitions can be "unique first-forbidden", "non-unique first-forbidden", "unique second-forbidden", etc. Experimental results of forbidden β-decays show that if the quantity K(E_e) defined in equation 1.11 is plotted against the electron energy E_e, in most cases these deviations are small small compared to a straight line plot , showing that forbidden transitions can be approximated to allowed transitions. Equation 1.10 can be still used to calculate decay rates of forbidden transitions, by adding an additional spectral shape factor term S(E_e) into the $f(Z, E)$ function, which represent the deviation of the electron energy spectrum from the allowed shape. It becomes:

$$\lambda = \frac{(4\pi)^2}{(2\pi)^5 c^6 \hbar^7} \; |M_{fi}|^2 \int_1^E \; E_e \; \sqrt{E_e^2 - 1} \; (E - E_e)^2 F(Z, E) S(E_e) \; dEe. \tag{1.15}$$

The "allowed approximation" will be used for decay rates calculations in section 4.2.

1.3 β-decay processes involving bound electrons

In the previous section, the β-decay was considered as a transformation of a nucleon in a nucleus, with an emission of an electron and an anti-neutrino for β^-, or a positron and a neutrino for β^+, both emitted particles going to the continuum. But the β-decay can also proceed by involving bound electrons of the atom. It will be described in the following.

1.3.1 Orbital electron capture

In the case of β^+, a positron is created, the energy needed to create this particle is $2{\cdot}m_e c^2$, thus restricting the energetically possible transitions to Q $\geq$ 1.022 MeV. In the other cases the transition will be possible only with the capture of an electron from the atomic orbits by a proton of the nucleus. The equation corresponding in the nucleon scale and in the atomic scale for this decay process are:

$$p + e^- \rightarrow n + \nu_e \tag{1.16}$$

$${}^{A}_{Z}X^{q} \rightarrow {}^{A}_{Z-1}Y^{q} + \nu_e, \tag{1.17}$$

and are equivalent to equations 1.2 and 1.4, respectively. This process, called orbital Electron Capture (EC), is competing with β^+ as the Q-value is getting smaller. As shown in equations 1.16 and 1.17, the emitted neutrino will get all the energy released by the transition, in contrary to the β^+ process where it has to share this energy with the positron, therefore it will have a well-defined energy (monochromatic).

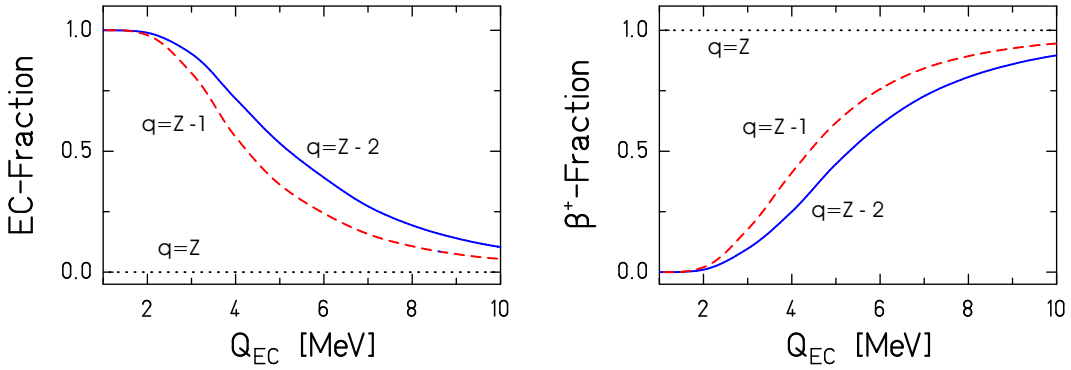

Figure 1.1: Comparison of the evolution of the relative fraction of the orbital EC (left) and the β^+ decay (right) as a function of Q-value, in the case of a nuclide with atomic number 82. The different lines represent different charge states of the atom, black dotted lines if fully-ionized, red dashed lines if hydrogen-like, blue solid lines if helium-like.

If all bound electrons are removed from proton-rich atoms, a direct consequence is that the EC channel is blocked, therefore only β^+ decay will be observed. Calculations [21] showing the relative fractions of β^+ and EC in a Z = 82 nuclide with 0 to 2 bound electrons is shown in figure 1.1. Measuring β^+ decay rates of fully-ionized atoms is one of the most promising methods to determine the respective branchings of the β^+ and EC channels, as it has been performed for ^{52}Fe and ^{53}Fe [8]. Also *unstable* fully-ionized atoms with Q-values smaller than $2{\cdot}m_e c^2$ will become *stable*.

1.3.2 Bound-state β-decay

The β^- decay process includes the creation of an electron. It can be imagined that the electron will go into a bound orbit of the daughter atom instead of going

into the continuum. It is called *bound-state* β-decay, a decay mode appearing in addition to the *continuum-state* β-decay observed in neutral atoms. In the nucleon scale it would correspond to the decay of a neutron to a *hydrogen atom*. The decay process is represented as the following in the atomic scale:

$$ {}^{A}_{Z}X^{q} \rightarrow {}^{A}_{Z+1}Y^{q} + \bar{\nu}_{e} \tag{1.18} $$

One can see that equation 1.18 represents the inverse of equation 1.17. This means that bound-state β-decay is the time-mirror process of orbital electron capture, and leads to the fact that these two processes can be described by the same nuclear matrix elements. Figure 1.2 illustrates the principles of orbital EC and bound-state β-decay.

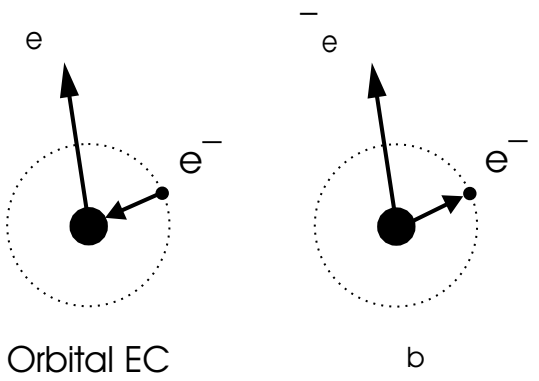

Figure 1.2: Schemes of orbital electron capture (left) and bound-state β-decay (right) in the atomic scale. Only the electrons involved in the decay processes are displayed.

The first description of this process was done in 1947 [10], and calculations has been performed for selected nuclides [22]. In neutral atoms, inner orbits (depending on the number of protons of the mother atom) are fully occupied, and due to the Pauli exclusion principle, the bound electron must go to higher orbits. It was calculated [22] that bound-state β-decay rate is smaller than 10^{-2} compared to continuum-state β-decay in the most favorable case for a neutral atom, the $^{3}\mathrm{H} \rightarrow {}^{3}\mathrm{He}$ transition. But by considering that all the electrons bound to the atom are removed, the probability of bound-state β-decay will drastically increase. The decay rate of the bound-state β-decay process can be determined as the following:

$$ \lambda \propto \sum_{x} \sigma_{x} \left|M_{fi}\right|^{2} \left|\psi_{e}^{x}(R)\right|^{2} E_{\bar{\nu}_{e}}^{2}, \tag{1.19} $$

where σ_x is the vacancy number of electrons at orbital x, $\left|\psi_{e}^{x}(R)\right|^{2}$ is the square of the wave function of the electron at orbital x, and $\mathrm{E}_{\bar{\nu}_e}$ is the total energy available for the anti-neutrino. The wave function can be scaled by a factor $\frac{(\alpha Z)^3}{n^3}$, which exhibits a strong dependance on the atomic number Z, and on the main quantum number n of the electron orbital x, such that the process is maximized for higher Z and if the inner orbits (especially the K-shell) are vacant. For calculations it is replaced by the maximum radial component of the relativistic electron wave function, either ψ_f or ψ_g [24], which modifies equation 1.19 as:

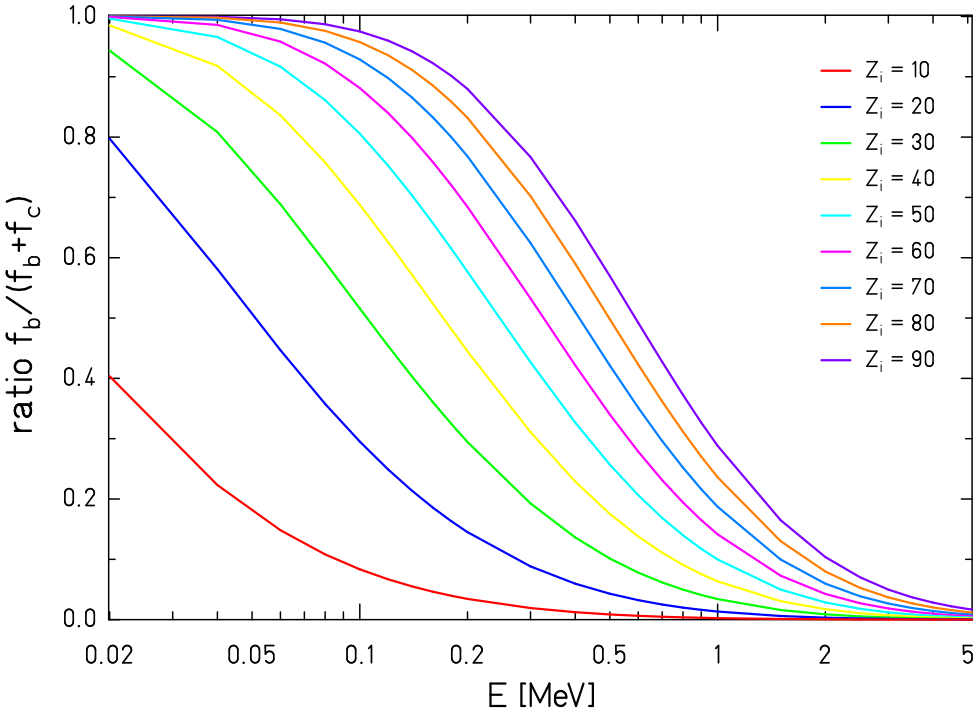

Figure 1.3: Calculations [23] of the ratio of the statistical rate function (f function described in section 1.2.3) of the bound-state β-decay to the sum of all f functions accounting for β-decay processes, as a function of the released energy E, for mother nuclides with atomic number ranging from $Z_i = 10$ to $Z_i = 90$.

$$\lambda \propto \sum_x \sigma_x \left|M_{fi}\right|^2 \left[max(\psi_f, \psi_g)\right]^2 E_{\bar{\nu}_e}^2 \tag{1.20}$$

The terms inside the sum (excluding the matrix element) is called the f function for the bound-state β-decay process, by analogy with the f function for the continuum-state β-decay process. The decay probability will increase for fully-ionized atoms, because the inner electron orbitals are available. The dependence on the square of the released energy, compared to the fifth power dependence as seen before for the continuum-state β-decay, shows that the latter process will be dominant for high Q-values, whereas bound-state β-decay dominates for smaller Q-values. Calculations [23] of the bound-to-total ratio of the f functions as a function of released energy E, for Z_i of mother nuclides ranging from 10 to 90, are displayed in figure 1.3. More details on these calculations are given in section 4.2.1. As mentioned in section 1.3.1, the ratio EC/β^+ has been already investigated experimentally [24], whereas the ratio β_b/β_c has not. The main goal of the experiments described in chapter 2 was to give *for the first time* such information.

1.4 β^--decay energetics for fully-ionized atoms

The Q-value of a reaction is determined from the mass difference between the daughter and mother nuclides involved in the reaction. The β^--decay equation 1.3 leads to:

$$Q_{\beta_c^-}^{q=0} = m_Y(A, Z+1) - m_X(A, Z), \tag{1.21}$$

which is valid for the decay of a neutral atom. This is also the Q-value for β^--decay which is given in literature, e.g. the total energy available for the leptons (rest mass and kinetic energy). If all the electrons are removed from the atoms, equation 1.21 is modified, which is equivalent as:

$$Q_{\beta_c^-}^{q=Z} = Q_{\beta_c^-}^{q=0} - \left|\Delta B_e^{tot}(Y, X)\right|, \tag{1.22}$$

where $|\Delta B_e^{tot}(Y, X)|$ is the difference of the total binding energy of the electrons between the mother and daughter nuclides (noted X and Y, respectively). This value varies from about 60 eV for light nuclides to 25 keV for heavy nuclides [25]. When considering the bound-state β^--decay process, the created electron goes to a bound orbital and gives some additional binding energy to the daughter nuclide. This leads to:

$$Q_{\beta_b^-,x}^{q=Z} = Q_{\beta_c^-}^{q=Z} + \left|B_e^x(Y)\right|, \tag{1.23}$$

where $|B_e^x(Y)|$ is the binding energy of an electron in orbital x of the daughter nuclide. The binding energy of an electron in the K orbital ranges from 13.6 eV for hydrogen to 157 keV for einsteinium [26], the heaviest element where β^- decay has been observed experimentally [27]. For medium or heavy masses, the influence of the electron "stripping" in the Q-value will therefore become important.

1.5 Astrophysical impact of β-decay

1.5.1 Stellar nucleosynthesis

How the chemical elements have been synthesized in the universe has been and still is one of the most crucial questions in nuclear astrophysics. The main problem was that thermonuclear fusion in stars could not be sufficient to produce elements beyond the Fe-Ni element region, because it was becoming energetically impossible. But it was proposed [28] that during the explosive stage of the stellar life, other nuclear reactions than fusion could occur and produce all observed elements in nature. The neutron and/or proton density, depending of the type of star investigated, could be so huge that consecutive neutron-capture or proton-capture competing with radioactive decays would lead to the population of all stable elements from Fe to U. The main evidence of this prediction was the discovery of technetium lines in the spectrum of the R Andromedae star [29]. The longest-lived isotope of this element (Tc is not observed on Earth) has a half-life on the order of 10^6 years. It was therefore produced inside the stellar medium, and gave the proof of nucleosynthesis in stars. Four main processes have been identified, proceeding by proton-capture (p-process and rp-process)

or by neutron-capture (s-process and r-process). Figure 1.4 shows the regions where these processes are observed (or predicted). The two processes involving neutron-capture will be described in more detail, especially the s-process.
The r-process stands for "rapid", in the sense that the neutron capture rate is expected to be very fast (on the order of ms) compared to radioactive decay rates. The stellar medium where it would occur would have a neutron density $n_n > 10^{20}$ cm^{-3} and temperatures T $> 10^9$ K [30]. Since it is competing with radioactive decays, the path of the r-process is going very far from stability. It is difficult to make good predictions on which radioactive nuclides are populated by this process, because many of them have not even been discovered, whereas they are expected to exist. The end-point of r-process is not known as well, but it is believed to be beyond the Th-U element region.

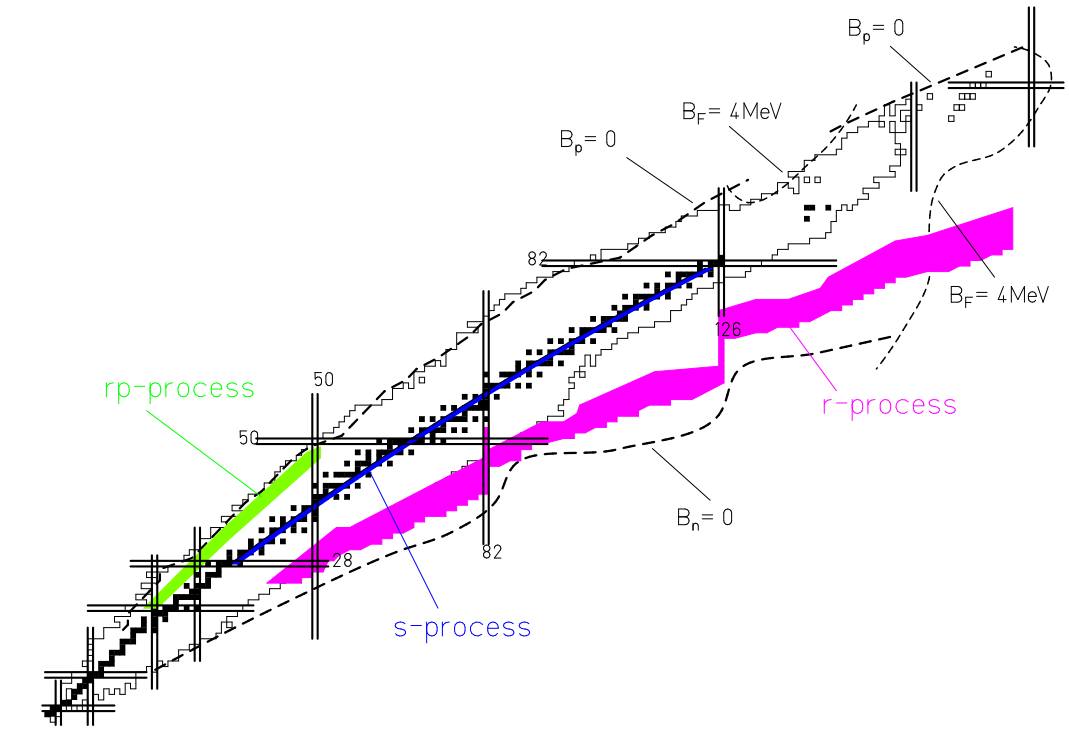

Figure 1.4: Path of the astrophysical processes through the chart of nuclides, indicated in green for rp-process, dark blue line for the s-process (close to the stable nuclides), and purple for r-process (mostly extrapolation, up to N = 180). The p-process is not shown but located close to the stable nuclides like the s-process. Stable nuclides are indicated in black.

1.5.2 The s-process

The s-process [31] represents the "slow" capture of neutrons, with a time interval in the range of 1 year to 10^6 years. From the competition between neutron capture and radioactive decays the path of the s-process is "forced" to follow the stable nuclides from ^{56}Fe (seed nuclide) to ^{209}Bi (endpoint nuclide). Further progress is highly improbable since there is not a known nuclear state with A = 211 having a half-life greater than hours [27]. The s-process has been divided into two components, depending on which region of the chart of nuclides it is

populating. In both cases the neutrons are coming from a (α,n) reaction with a nuclide produced by the CNO cycle. The weak component populates nuclei with A $<$ 90, with a neutron flux of about 7×10^5 cm^{-3} at a temperature of approximately 3×10^8K corresponding to 30 keV [31]. The neutrons are coming from the ^{22}Ne(α,n)^{25}Mg reaction. The strong component applies for nuclei with A $>$ 90, with a neutron flux of approximately 4×10^8 cm^{-3}, the temperature being around 0.9×10^8 K or 10 keV [31]. In this case the neutrons are originating from the ^{13}C(α,n)^{16}O reaction. Some elements with large abundances are observed at neutron magic numbers N = 50, 82, 128 corresponding to elements with A $\approx$ 90, 140, 208.
This process is predicted to happen in some specific class of stars called AGB (Asymptotic Giant Branch) stars also known as red giants, during the explosive He burning phase. The two main ingredients needed to determine a s-process path and calculate element abundances are neutron-capture rates and lifetimes. From the temperature and pressure expected to occur inside such objects, the majority of the electrons normally attached to the atom are excited from their bound orbits, which can lead to dramatic changes in lifetimes. This can create some branching or even change the path of s-process for some specific nuclides.

1.6 Experiments on bound-state β-decay

During the last fifteen years decisive progress has been made in the possibility to observe the bound-state β-decay process. This was mainly due to the feasibility to store a large number of fully-ionized atoms (up to 10^8) for a long period of time (up to hours). In the following two prominent examples of lifetime modification by electron stripping will be described.

1.6.1 The ^{163}Dy experiment: first observation of bound-state β-decay

The first nuclide where bound-state β-decay was observed experimentally was ^{163}Dy [32]. According to nuclear data tables, this nuclide is supposed to be *stable*, with a Q-value for the continuum-state β-decay process $Q_{\beta_c^-}^{q=0}$ = -2.555(16) keV [27]. But this is only valid for the *neutral* atom. If the atom is *fully-ionized*, the Q-value for continuum-state β-decay is modified by the difference between the total binding energies of the electrons in the mother and daughter atoms [25]. Using equation 1.22 leads to:

$$Q_{\beta_c^-}^{q=66} = -2.555(16) - 12.493 = -15.048(16)\ keV, \tag{1.24}$$

which means that the continuum-state β-decay of ^{163}Dy^{66+} is *forbidden*. Considering the bound-state β-decay process, the binding energy of the orbital electron of the daughter nuclide has to be added. For an electron bound in the K or L shell [26], equation leads to 1.23:

$$Q_{\beta_b^-(K)}^{q=66} = -15.048(16) + 65.137 = 50.089(16)\ keV, \tag{1.25}$$

$$Q_{\beta_b^-(L)}^{q=66} = -15.048(16) + 16.562 = 1.514(16)\ keV. \tag{1.26}$$

The bound-state β-decay of $^{163}Dy^{66+}$ is *allowed* with a electron going to the K or L orbitals. An experiment at the GSI facility was carried out to detect the decay products of $^{163}Dy^{66+}$ [32]. Since the mass difference between $^{163}Dy^{66+}$ and $^{163}Ho^{66+}$ is very small, a special technique was used to detect only the daughter nuclides. Up to 10^8 $^{163}Dy^{66+}$ ions were injected into the ESR with an energy of 294 MeV/u during an accumulation period. Thereafter a small fraction of the $^{163}Dy^{66+}$ ions which had decayed to $^{163}Ho^{66+}$ during the accumulation period were purged by their crossing with an argon gas jet target, which resulted in the stripping of the K electron in $^{163}Ho^{66+}$. The remaining $^{163}Dy^{66+}$ ions were stored and cooled for a variable period of time. The measurement of the decay products was possible by another application of the gas jet target, which stripped again the K electron in $^{163}Ho^{66+}$. The $^{163}Ho^{67+}$ ions produced by the stripping were identified with a position-sensitive particle counter the $^{163}Ho^{67+}$ ions produced by the stripping. At the same time the mother nuclides were also detected with another position-sensitive particle counter. The bound-state β-decay rate was derived with the following equation (taken from ref. [32]):

$$\frac{N_{Ho}(t) - N_{Ho}(t=0) \cdot e^{-\lambda_{tot}^{Ho} t}}{N_{Dy}(t)} = \lambda_{\beta_b} \cdot t \cdot \left(1 + \frac{(\lambda_{tot}^{Ho} - \lambda_{tot}^{Dy}) \cdot t}{2} + ...\right), \qquad (1.27)$$

where $N_{Ho}(t)$ and $N_{Dy}(t)$ are the number of $^{163}Ho^{66+}$ and $^{163}Dy^{66+}$ after storage time t (starting from the first application of the gas jet target), respectively. λ_{β_b} is the decay constant for bound-state β-decay of $^{163}Dy^{66+}$. λ_{tot}^{Dy} and λ_{tot}^{Ho} are the total decay constants of $^{163}Dy^{66+}$ and $^{163}Ho^{66+}$ respectively. In first order the number of $^{163}Ho^{66+}$ ions that have been produced during time t by bound-state β-decay, normalized to the mother ions, is proportional to the bound-state β-decay constant. By measuring this number after different storage times, from 10 min to 85 min, the bound-state β-decay constant was derived as $\lambda_b = 1.68(10) \times 10^{-7}$ s^{-1} and the half-life as:

$$T_{1/2} = 48(3)\ d. \qquad (1.28)$$

This showed that a *stable* nuclide could become *unstable* only by removing the bound electrons from the atom. This result had an astrophysical impact in the abundance problem of ^{164}Er [33], which could be produced in the s-process from the decay of ^{163}Dy, neutron capture of ^{163}Ho and decay of ^{164}Ho. In this case the s-process path was modified on the mass region 163-166. In addition boundaries could be evaluated *for the first time* for the mass of the *neutrino*, from the ratio of the electron capture from M1 and M2 shells in neutral ^{163}Ho [34, 35] to the bound-state β-decay of fully-ionized ^{163}Dy, as $m_{\nu_e}c^2 \leq 275$ eV. This boundary is still far from the one obtained for the *antineutrino* of 2.8 eV [19] mentioned before.

1.6.2 The ^{187}Re experiment: study of a cosmological clock

The ^{187}Re-Os pair has been proposed [36] as one of the cosmological "clocks" to determine the lower limit of the age of the universe. But Yokoi *et al.* [37] suggested that the half-life of ^{187}Re could be strongly affected by the stellar medium, because the removal of the bound electrons would modify enough the Q-value of

the ^{187}Re β-decay to make possible the *non-unique first-forbidden* transition of the $5/2^+$ ground state of $^{187}Re^{75+}$ to the $3/2^-$ excited state of $^{187}Ho^{75+}$ at 9.746 keV [38], overshadowing the *non-unique second-forbidden* transition to the $1/2^-$ ground state of $^{187}Ho^{75+}$, which is exclusively observed in the decay of neutral ^{187}Re.

This new transition would be possible for $^{187}Re^{75+}$ only via bound-state β-decay, with the electron going into the K shell, whereas all continuum-state β-decay channels would be blocked. A half-life prediction of 14 years has been performed [39] using a *log-ft* value of 7.5 for this transition. It was much reduced compared to the literature value of $4.12(2) \times 10^{10}$ years for the neutral atom [40]. This change has a drastic influence on the determination of T_N^{min}, the time duration of the star formation and nucleosynthesis until the formation of the protosolar nebula, this value being determined from the abundances at T_N, decay rates and production probabilities of ^{187}Re and ^{187}Os. A value $T_N^{min} = 11.5 \times 10^9$ yr has been deduced from the decay constant of the neutral decay constant of ^{187}Re. It would be modified by taking into account an effective decay constant resulting from the contribution of bound-state β-decay in the highly-charged ^{187}Re. To have a reliable value for this effective decay rate, an evaluation of the decay of fully-ionized ^{187}Re is necessary.

An experiment was performed to measure the decay rate of $^{187}Re^{75+}$ [41]. These ions were produced by the stripping through a copper foil of $^{187}Re^{50+}$, coming from SIS with an energy of 347 A·MeV, and injected into the ESR. The procedure to measure the number of $^{187}Re^{75+}$ ions and their decay products was similar to the one performed for $^{163}Dy^{66+}$ described in subsection 1.6.1. The $^{187}Re^{75+}$ ions were accumulated (up to 10^8), and after a variable time the $^{187}Os^{75+}$ ions produced by bound-state β-decay were stripped from their electron by the application of a gas jet target. Thereafter the $^{187}Os^{76+}$ ions were measured independently by a position sensitive detector and with Schottky Mass Spectrometry [42]. The half-life of $^{187}Re^{75+}$ was determined from the average of the two measurements as:

$$T_{1/2} = 32.9(2.0)\ yr, \tag{1.29}$$

being reduced by about nine orders of magnitude compared to the half-life of the neutral atom of $4.12(2) \times 10^{10}$ years [40]. The result was slightly different from the predictions, but this was mainly due to a large uncertainty in the estimation of the *log-ft* value for the (previously) unknown transition. From the recalculated effective half-life of ^{187}Re the resulting T_N^{min} was reduced by about 1 Gyr.

Chapter 2

Experiments with fully-ionized atoms

2.1 Production of highly-charged exotic nuclides

Exotic nuclides are short-lived and therefore they are not found in terrestrial environment. They can be produced from stable nuclides via different nuclear reactions, the main being fragmentation, fission and fusion [43]. Fusion is the only process applicable to produce very heavy nuclides beyond uranium [44], whereas fission and fragmentation are used to populate all possible species lighter that this element. In the following only projectile fission and fragmentation are described.
Projectile fission is a process where a heavy projectile nuclide is subject to induced fission when excited by the collision with a target, with two main fragments produced. This process is competing with the electromagnetic dissociation, depending on the target and projectile energy. The most commonly used nuclides for this process are the stable isotopes of uranium, where the spontaneous fission probability becomes non negligible and the range of fragments populated is the largest. The fission process can be symmetric, the distribution of fission fragments being distributed in the element range from about $1/4 \cdot Z_{proj}$ to about $3/4 \cdot Z_{proj}$, with a maximum in atomic number near half of the projectile atomic number. The fission process can also be assymetric with two maxima in the mass distribution of the fission fragments, at about $1/4 \cdot Z_{proj}$ and $3/4 \cdot Z_{proj}$, and a minimum at half the projectile mass. From the principle of fission (two fragments produced) these fragments have a mass far from the projectile mass. Since highly-charged ions are involved in these reactions, the Coulomb repulsion between the two fission fragments leads to the fact that they will have a different velocity than the one of projectile.
The projectile fragmentation can be represented as a two-step process where the projectile is losing a variable number of nucleons by interacting with a light target. In the first step, called *abrasion*, nucleons are removed from the projectile, leading to the formation of prefragments. The second step, called *ablation*, follows with the deexcitation of the prefragments by evaporation cascade of nucleons. The fragments will have a similar velocity that the one of the projectile. The production yield of the fragments decreases with the increasing number of nucleons removed. These two processes are complementary in the population of fragments, and also in the kinematics, in order to produce a wide range of exotic nuclides.

The angular momentum distribution of any fragment, which leads to the production probability of isomeric states by such reaction, depends on a first approximation on the number of nucleons removed from the projectile in order to produce this fragment. This assumption is important for the calculations performed in section 5.2.
At the energies used for the reactions mentioned above, the fragments or fission fragments are partially or fully ionized (depending on the binding energy of the electrons, thus to the atomic number of the fragments). To be able to remove all remaining electrons from the created fragments (or fission fragments), thin stripper foils are necessary. Material such as neobium or copper is used. In order to study a particular fragment (or a selected cocktail of fragments) separation of this fragment from the other contaminants is necessary. The FRS-ESR combination is described in the following.

2.2 Combination of the in-flight separator FRS and the storage cooler ring ESR

2.2.1 Properties of the in-flight separator FRS

The fragment separator FRS [45] is an magnetic spectrometer which has been designed [46] to separate efficiently fragments produced by a nuclear reaction. It has a transmission acceptance in magnetic rigidity Bρ of about $\pm$ 1 % for centered fragments The experiments described in the following use two methods of separation, the Bρ - ΔE - Bρ separation and the pure magnetic rigidity analysis. With this two techniques selected cocktail beams or mono-isotopic secondary beams can be produced.
The first method relies on the fact the the energy loss ΔE of a given nuclide passing through matter is proportional to Z^2 [47, 48], the square of the atomic number of this nuclide. The first part of the FRS is used to separate the fragments according to their magnetic rigidity Bρ, this quantity being related with the magnetic field B of the magnets of the FRS, the mass-over-charge ratio (m/q) and velocity v of the fragments, as:

$$B\rho = \frac{\gamma m v}{q}. \tag{2.1}$$

After the first stage of the FRS a degrader will separate the fragments with Z. The second stage of the FRS completes the separation with Bρ. Slits are also placed at different locations of the FRS to stop the undesired fragments. A sketch of the FRS showing the principle of the Bρ - ΔE - Bρ is presented in figure 2.2
The pure magnetic rigidity analysis relies on the separation only by means of Bρ. From the fragmentation process all the fragments have a similar velocity, therefore a selection in mass-over-charge ratio (m/q) of the fragments can be performed. The separation of two isobars with a similar m/q is less efficient as in the Bρ - ΔE - Bρ method, but has a better overall transmission for the fragments.

2.2.2 Storage cooler ring ESR

After the separation of the fragments of interest, they can be injected into the ESR [49] for further studies. The cooler storage ring ESR has a circumference

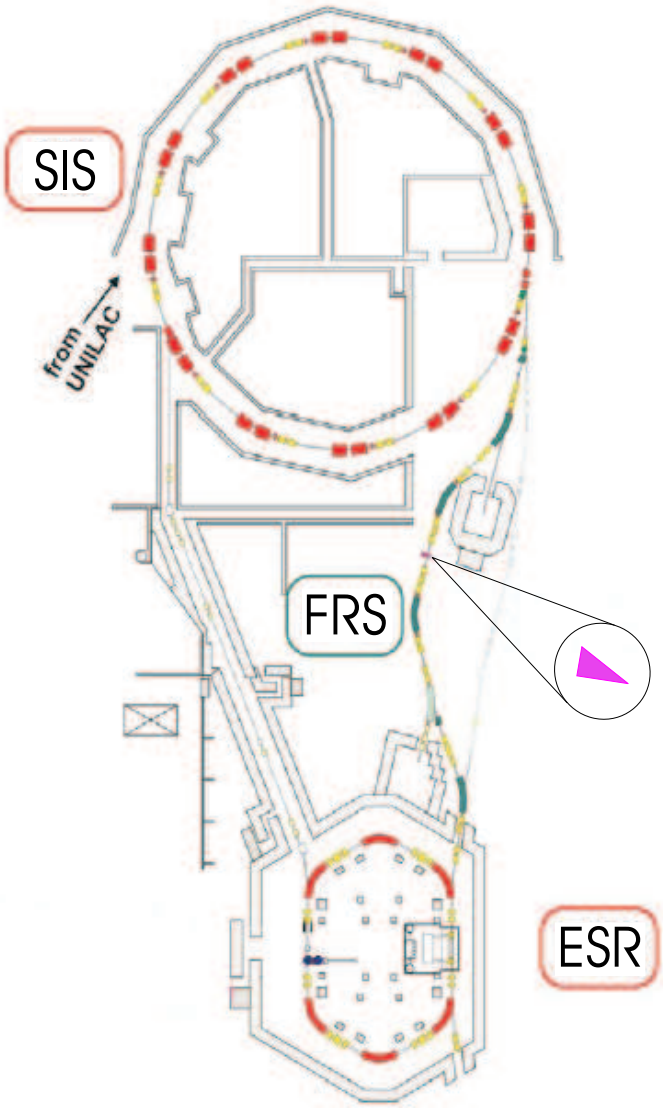

Figure 2.1: Part of the GSI facility, including the heavy-ion synchrotron SIS, the in-flight separator FRS and the storage cooler ring ESR. The degrader used for the Bρ - ΔE - Bρ separation, located in-between the two stages of the FRS, is zoomed.

of about 108.36 m. It has a injection acceptance from the FRS of about $\pm$ 0.2 % in Bρ, and storage acceptance of about $\pm$ 1.5 %. The fragments injected into the ESR having a similar Bρ, a difference in theit mass-over-charge will lead to a difference in their velocity. To reduce this difference in velocity and also to reduce the velocity distribution of any fragment (about $\Delta v/v \sim 10^{-3}$), a cooling system is necessary. It is described in the following section with the method used to study the circulating ions into the ESR, the Schottky Mass Spectrometry.

2.2.3 Schottky Mass Spectrometry

After the injection into the ESR, time-resolved Schottky Mass Spectrometry (SMS) [42] was applied to the fragments. It is based on the fact that each ion circulating into the ESR has a specific frequency revolution which is related to

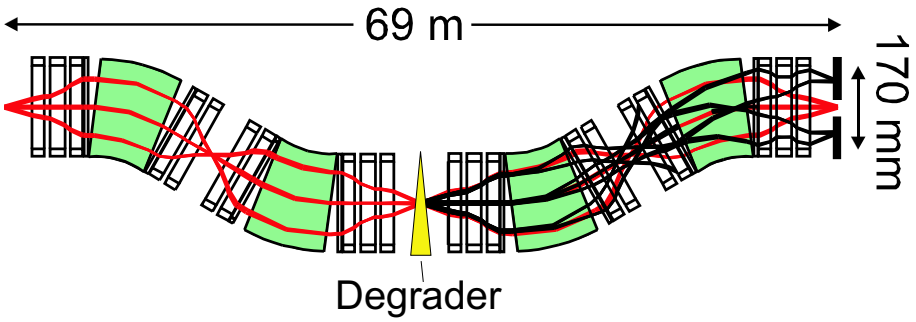

Figure 2.2: Principle of the Bρ - ΔE - Bρ separation method. A mixture of two isobaric fragments is getting through the first stage of the FRS without being separated (in red). A degrader placed in the middle of the FRS displace one of the two fragments from the other one due to their different energy-loss. The second stage of the FRS achieve the separation of the two fragments (in red and in black) with the help of slits.

its mass-over-charge ratio. The frequency revolution of two different ions species are related by [50]:

$$\frac{f_j - f_i}{f_i} = \eta \, \frac{p_j - p_i}{p_i} = \left(\frac{1}{\gamma^2} - \alpha_p \right) \frac{p_j - p_i}{p_i}, \tag{2.2}$$

where i and j are the index of two different ion species, f, p and γ are the mean frequency, the momentum and the Lorentz factor of the ion species, respectively. The momentum compaction factor α_p is defined as:

$$\alpha_p = \frac{dC/C}{d(B\rho)/B\rho}. \tag{2.3}$$

It represents the variation of the orbit length C with variation of magnetic rigidity Bρ. It depends on the optical and field settings of the ESR. The dependence of the revolution frequency difference between two ions with mass, charge and velocity difference is:

$$\frac{f_j - f_i}{f_i} = -\alpha_p \frac{(m/q)_j - (m/q)_i}{(m/q)_i} + \frac{\Delta v}{v} \left(1 - \alpha_p \gamma^2 \right), \tag{2.4}$$

where m/q and v = βc and γ = (1 - β^2)$^{-1/2}$ are the mass-over-charge ratio, the velocity and the Lorentz factor, respectively. If the velocity distribution is sufficiently small (Δv/v < 10^{-6}), the second term of equation 2.4 can be neglected and it becomes:

$$\frac{f_j - f_i}{f_i} = -\alpha_p \frac{(m/q)_j - (m/q)_i}{(m/q)_i}. \tag{2.5}$$

Electron cooling [51] is applied to the fragments circulating into the ESR in order to reduce the velocity distribution of these fragments and force them to circulate with a fixed velocity, determined only by the electron cooler high voltage U_{cooler} from the following relations:

$$E_e^{kin} = m_e c^2 (\gamma - 1) = e U_{cooler}, \tag{2.6}$$

$$\gamma = 1 + \frac{U_{cooler}}{m_e c^2}. \quad (2.7)$$

Small corrections depending on the electron cooler current have to be taken into account (see section 4.1.2 for actual calculations). The cooling force depends on the number of particles to be cooled, and on the difference in velocity between the cold electrons and the ions, as $F \propto \Delta v^{-3}$. In principle the cooling process can take infinite time to be in complete equilibrium with the intra-beam scattering, but in practice the reduction of the relative velocity distribution of the ions down to few 10^{-7} takes from 30 to 100 s.
By recording the signal induced by the cooled ions through pick-ups electrodes at every turn into the ESR, and by applying a Fourier transform to this signal, in the frequency spectra obtained peak structures will correspond to specific ion species. The area of any frequency peak is proportional to the number of ions related to this peak, as well as to the square of their ionic charge [52]. It has been proved by reproducing experimentally the calculated half-lives of fully-ionized atoms [8, 9]. Since the data are continuously recorded, the analysis of frequency spectra produced at different times after the injection into ESR will permit to derive the time evolution of any ion species.

2.3 Decay study experiments on ^{207}Tl

2.3.1 Motivation for the decay study of ^{207}Tl

Previous experiments (see section 1.6) which studied bound-state β-decay of "stable" projectiles only measured the decay rate of nuclides where this process was the only energetically possible, with continuum-state β-decay being blocked. The goal of our new experiment is to measure the decay rate of a nuclide where both β-decay channels are allowed, in order to measure their respective branchings. The mother ions, as well as the daughter ions produced by bound-state β-decay would be measured simultaneously with time-resolved Schottky Mass Spectrometry (SMS) [42]. We have chosen ^{207}Tl because it fulfills many requirements to have an optimum measurement of the bound-state β-decay process.
The Q-value of the bound-state β-decay process should be large enough to resolve the mother and daughter ions with SMS, since they have a similar m/q ratio ($m/\Delta m < 600000$). The Q-value should be also small enough to have a observable bound-state β-decay branching, since this branching increase with decreasing Q-value (see section 4.2.1 for more details). It should not be too small, to be able to measure the decay of mother ions within a reasonable observation time, between 30 min to 1 hour, because the decay rate is proportional on a first order to Q^5 for continuum-state β-decay, and Q^2 for bound-state β-decay. The half-life of the nuclide should be much longer than the cooling time necessary to reduce its momentum spread (less than 10 s), but not too long because else wise the non-nuclear processes would dominate the decay of mother ions (beam lifetime less than 1 h, see section 4.1.2 for details). The nuclide should have a atomic number Z as high as possible, because the bound-state β-decay rate is roughly proportional to Z^3, and a large production yield. For the latter condition a nuclide produced by projectile fragmentation, with very few nucleons removed from the projectile, would be suitable.

^{207}Tl has a atomic number Z = 81, a half-life of 286(2) s [53], a Q-value for β^--decay of 1418(5) keV [27], and corresponds to the one-proton-removal channel in the projectile fragmentation of ^{208}Pb. As it will be shown in section 4.2.1, it has an expected significant branching for bound-state β-decay (about 15 %, see figure 1.3). Also its decay scheme is very well known [55], which allows to predict the half-life of this nuclide if fully-ionized as it will be performed in section 4.2.2.

2.3.2 First direct observation of bound-state β-decay

An experiment was carried out to investigate the decay properties of $^{207}Tl^{81+}$ ions. These ions were produced from a projectile fragmentation of a ^{208}Pb beam in a thick Be target. This beam was provided by the GSI accelerator facility. A ^{208}Pb beam was accelerated in the Universal Linear Accelerator (UNILAC) up to 11.1 MeV/u. The partially ionized $^{208}Pb^{67+}$ were injected into the heavy-ion Synchrotron (SIS) to be accelerated up to 838 A MeV, corresponding to a magnetic rigidity B_ρ = 15.58 Tm. ^{207}Tl fragments were produced by a collision of this projectile in a 4 g/cm^2 Be target nuclide. Thereafter they were separated by the Fragment Separator FRS [45, 46], with the ΔE-Bρ-ΔE method, in order to remove the contamination of the other ions that were produced during the fragmentation process, especially the $^{207}Pb^{81+}$ ions which are the bound-state β-decay daughters of $^{207}Tl^{81+}$. For this a wedge shaped degrader was put between the two stages of the FRS. The $^{207}Tl^{81+}$ ions were injected into the ESR [49] with an energy of 400.5 MeV/u and a relative momentum distribution of about 10^{-3}. This rather large distribution was reduced with the application of electron cooling. The ions circulating into the ESR were merged with a cold electron beam with a fixed velocity, and the ions were forced to circulate into the ESR with the same velocity, which led to the reduction of the momentum distribution down to 5×10^{-7} by interaction with the electron beam.
The data acquisition system is presented in figure 2.6. The Schottky noise was recorded by the "Sony Tektronix 3066 Spectrum Analyzer" [56](described in section 3.1.2). The frequency revolution of the $^{207}Tl^{81+}$ ions circulating into the ESR was about 1.975 MHz. The 30th harmonic of this frequency was used, leading to a frequency of about 59.25 MHz. A frequency offset (or local oscillator offset) was applied in order to be able to measure the Schottky noise with reasonable sampling frequencies (about 2 to 5 kHz).

2.3.3 Improved experiment on $^{207}Tl^{81+}$

The first experiment which studied the bound-state β-decay of $^{207}Tl^{81+}$ (presented in ref. [57]) showed that the estimation of the bound-state β-decay constant were strongly dependent on the time right after the injection of the fragments into the ESR. The first 100 s had been necessary for the electron cooling system to reduce the relative momentum distribution of the ions down to 5×10^{-7}, the corresponding data had been therefore excluded from the analysis. Also there were problems with the cooling efficiency, probably due to a misalignment of the ions and the electron beam, which led to unstable decay of $^{207}Tl^{81+}$.
In order to improve the results, a new experiment was carried out, similar in principle to the first one, but with new cooling conditions. The $^{207}Tl^{81+}$ ions were produced by projectile fragmentation of 704.8 MeV/u ^{207}Pb on a 4 g/cm^2

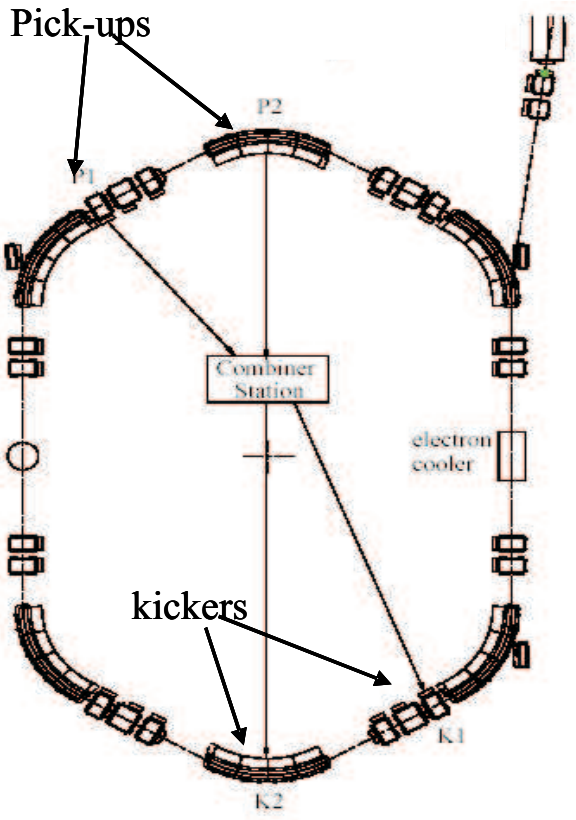

Figure 2.3: Scheme of the ESR with the pick-up electrodes, combiner station and kicker stages indicated.

Be target. The $^{207}Tl^{81+}$ fragments were separated by the FRS using pure Bρ separation, and injected into the ESR with an energy of 401.4 MeV/u. In addition to the electron cooling system, the stochastic precooling system [58] was applied, *for the first time* for fragments. It consists on pick-up electrodes which record the signal induced by the circulating ions, combine their information, and send a signal to kicker stages in order to correct the momentum spread of the ions. The whole process can reduce the relative momentum distribution of the circulating ions from values (5×10^{-4} - 10^{-3}) at the injection down to about few 10^{-5} in less than 5 s. The latter value cannot be reduced due to heating processes which equilibrate with cooling processes. To reduce furthermore the momentum distribution the electron cooling is still necessary, but it is much more effective when starting from values as 10^{-5}, and reduces the relative momentum distribution down to about 5×10^{-7}.

Figure 2.4 illustrates the cooling process by a three-dimensional plot of the intensity evolution of the $^{207}Tl^{81+}$ ions with time on the top part. The relative momentum distribution is plotted on the same time scale on the bottom part. The stochastic precooling enters into operation about 1 s after the injection, until 3.5 s after the injection. After 3 s the relative momentum distribution reaches an equilibrium at about 3×10^{-5}. After 3.5 s only the electron is in operation, and 3 s later the relative momentum distribution is reaching a new equilibrium at about 5×10^{-7}. The total time needed to reduce the relative momentum distribution down to this value is 6 to 7 s from the injection time. The electron

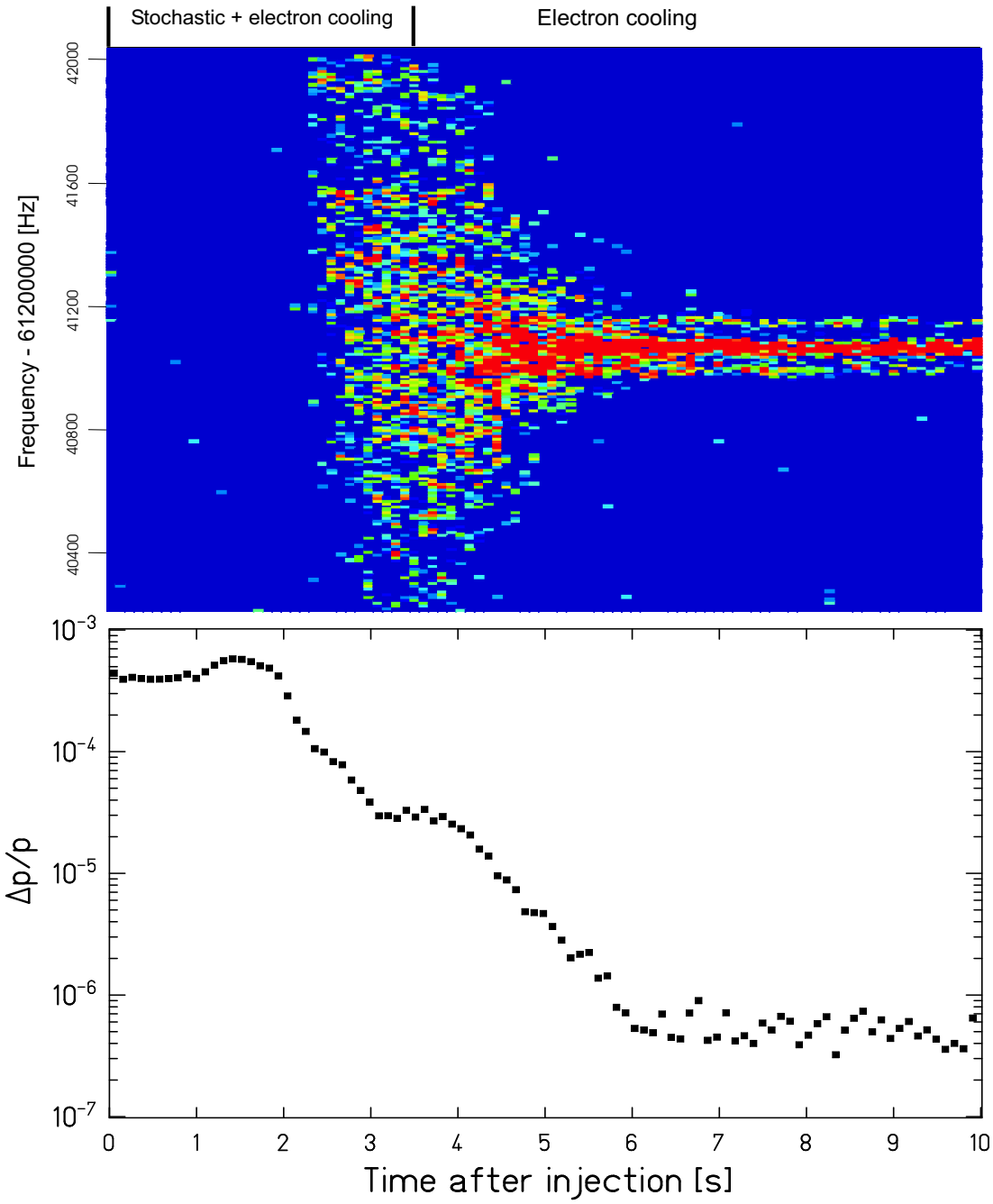

Figure 2.4: Example of injection with the application of stochastic precooling in addition to electron cooling. Top: time-evolution of the intensity of $^{207}Tl^{81+}$ ions, the intensities values are marked with a colour code. Bottom: corresponding evolution of the relative momentum distribution of these ions.

cooling was continuously applied during the measurement. This cooling time is much reduced compared to the typical values of 30 to 100 s obtained by using only the electron cooling system [57, 59]. The parameters for the electron cooler were $U_{cooler} = 220020$ V and $I_{cooler} = 100$ mA, leading to a velocity $\beta = 0.715$. The contamination of the $^{207}Pb^{81+}$ ions injected in the ESR was kept to a low level (1.5 % on average) compared to the number of $^{207}Tl^{81+}$ ions injected at the same time, as it is shown in figure 2.5. This number is slightly higher than the one obtained in the first experiment of about 1 %, where the ΔE-Bρ-ΔE had

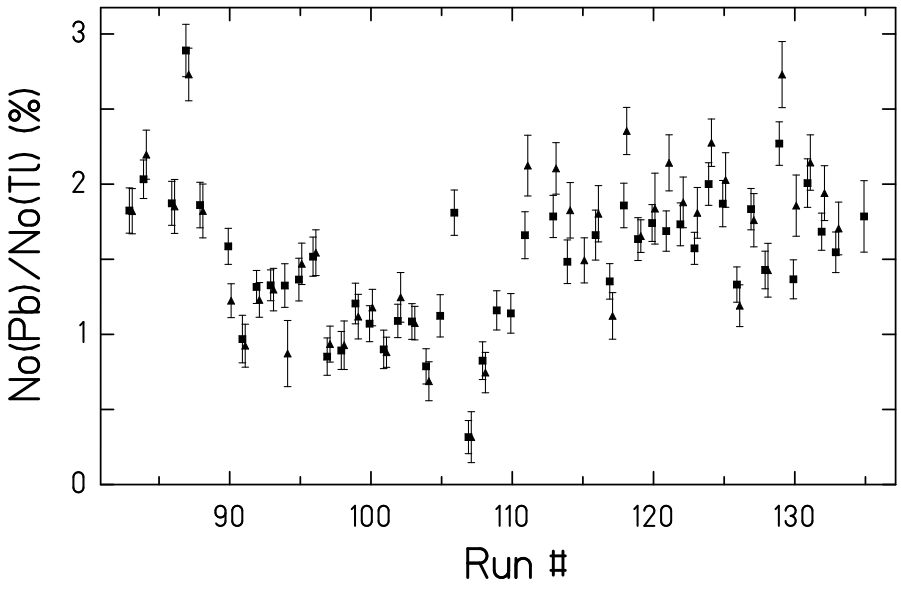

Figure 2.5: Ratio of the initial number of $^{207}Pb^{81+}$ ions to the initial number of $^{207}Tl^{81+}$ ions injected into the ESR for each injection, with squares for SONY data and triangles for TCAP data. The results from both acquisition systems are consistent with each other.

been used. This result allows a maximal sensitivity of the evolution of $^{207}Pb^{81+}$ to the feeding from the bound-state β-decay of $^{207}Tl^{81+}$, which is the most intense right after the injection. The $^{207}Tl^{81+}$ and $^{207}Pb^{81+}$ ions evolution was measured with the data acquisition system described in section 2.3.4. The $^{207}Pb^{82+}$ ions have been monitored by a particle detector located after a dipole magnet of the ESR.

2.3.4 Data acquisition

The Schottky noise was recorded simultaneously by the "Sony Tektronix 3066 Spectrum Analyzer" (described in section 3.1.2) and a Time Capture (TCAP) system (described in details in ref. [60]). The revolution frequency of the $^{207}Tl^{81+}$ ions is about 1.975 MHz, and the 31st harmonic of this frequency was used, leading to a frequency of about 61.24 MHz. A frequency offset was applied in order to be able to measure the Schottky noise with smaller sampling frequencies. The signal was sampled by an 16-bit ADC with a sampling frequency of 640000 Hz, and stored into disk. In addition a particle counter was placed in the inner part of the aperture of the ESR. It was dedicated to record the $^{207}Pb^{82+}$ ions, the continuum-state β-decay daughters of $^{207}Tl^{81+}$. The detector also stopped these ions in order to avoid contamination of $^{207}Pb^{81+}$ by radiative electron recombination from the cooler.

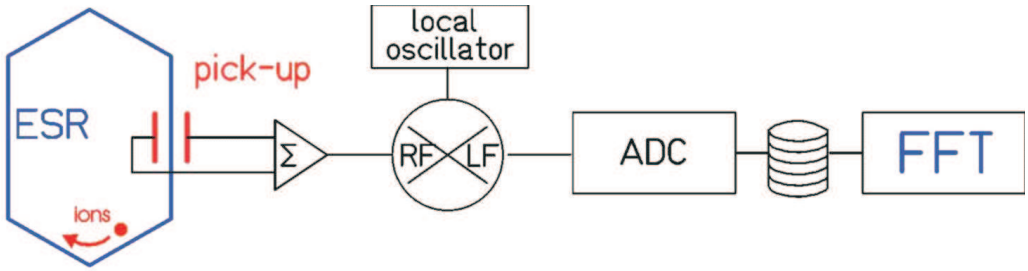

Figure 2.6: Description of the data acquisition system. The periodic revolution of the ions circulating into the ESR are recorded by pick-up electrodes, the signal is down-mixed with a local oscillator frequency, digitized by a 16-bit ADC, and recorded to disk. A FFT can be applied to the data to monitor the signals on-line or to analyse them off-line.

Chapter 3

Data Analysis

3.1 Fourier Analysis of raw data

3.1.1 Principle

By recording the periodic signal induced by the ions circulating into the ESR, a Fourier transform applied to the time-domain signal will lead to a frequency-domain signal which exhibit information on the circulating ions. The Fourier analysis proceeds as follows:

- An window function is applied to the digitized amplitudes of one data block.
- The "windowed" amplitudes of one data block are Fourier-transformed with the equation of the type:

$$H_n = \sum_{k=0}^{N-1} h_k e^{\frac{2\pi i k n}{N}} \tag{3.1}$$

  , where n, k are integers, N the number of samples per block.

- The noise power density amplitudes obtained are averaged over different blocks to improve the signal-to-noise ratio, assuming that the following relation applies to the noise background, as it has been checked and verified in ref. [61]:

$$\frac{\sigma_A}{A} = \frac{1}{\sqrt{N_{aver}}}, \tag{3.2}$$

where A is the intensity of one channel in the frequency spectrum, σ_A the standard deviation of this intensity, N_{aver} the number of blocks averaged to produce the frequency spectrum studied. Figure 3.1 shows the principles of Fourier analysis. A special algorithm, the so-called Fast-Fourier Transform (FFT), was used in order to decrease the computer time needed to perform the Fourier transform. Due to a limited number of samples recorded during the acquisition, the application of a window function to the data is necessary to avoid the appearance of strong side lobes around the true frequency peaks ("leakage") after the Fourier transform. The windows used in the following are the Hamming and Hanning windows. Applying a window function means also that part of the original data

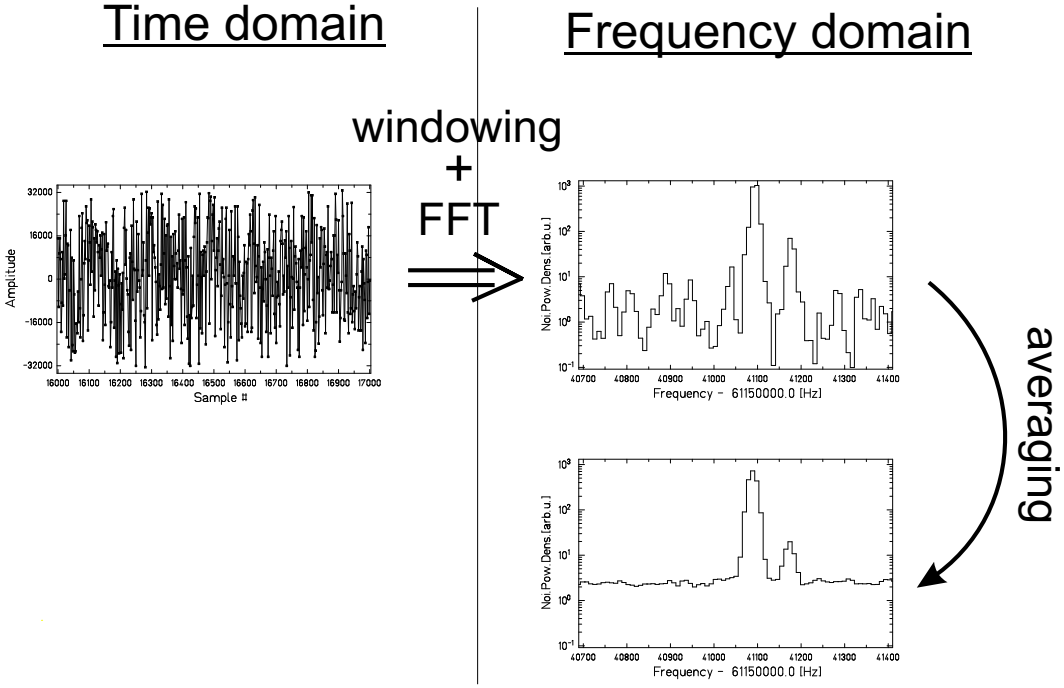

Figure 3.1: Schematic example of the Fourier analysis. To the noise amplitudes (only a part of one data block is shown) are applied a window function, then they are Fourier-transformed with a FFT algorithm. Several frequency spectra are averaged to optimize the signal-to-noise ratio.

is discarded before the FFT occurs. The smoother the window is, the more data is discarded. The choice of the window must balance these two problems.
As explained in section 2.3.4, the data was recorded simultaneously by two acquisitions systems, called "SONY" and "TCAP". Treatment of the data for each system is similar in principle, but will be explained separately.

3.1.2 Fourier analysis in the SONY Spectrum Analyzer

For the following the denomination *frame* is preffered to the block, to be consistant with the system interface and manual [56]. The "SONY TEKTRONIX 3066 Spectrum Analyzer" [56] has a built-in FFT algorithm, such that the frames are already being processed during the acquisition of the data. The user can set parameters to control how the FFT will be performed before the acquisition starts. These parameters are the number of FFT points in one frame, the span (the bandwidth used by the FFT), the frequency offset FO (start of the frequency range after the FFT, such as f(FFT) = f - FO), the frame length which depends on the span, the frame period and the number of frames.
The frame length is the time duration of the acquisition of one frame, and the frame period is the time interval between the start of the acquisition of two consecutive frames. If the frame period is set to be smaller than the frame length, there is some overlap in the time domain between the acquisition of two (or more) frames. There is also a lower limit to the frame period depending on the span, determined by the fact that no more than 64 frames can be recorded in parallel at a given time.

The parameters used in the 1st experiment were:

- Span 2 or 1 kHz
- Frequency Offset 59000000 Hz
- Frame Length 320 or 640 ms
- Frame Period 240 or 480 ms
- Number of frames 2000 or 4000
- Hamming Window

The parameters used in the 2nd experiment were:

- Span 1 kHz
- Frequency Offset 61240000 Hz
- Frame Length 640 ms
- Frame Period 480 ms
- Number of frames 4000
- Hamming Window

The Hamming window corresponds to a function:

$$w(k) = 0.54 - 0.46cos\left(\frac{2\pi k}{N}\right), \tag{3.3}$$

applied to the raw data, where N is the total number of samples per data block, and k the current sample number in the data block.
Frequency spectra have been generated by averaging 30 consecutive frames, having a total time duration of 14.56 s. This averaging time was chosen because only the first spectrum includes the cooling process, complete after about 7 s, and the decay of the isomeric state of $^{207}Tl^{81+}$, which has vanished after about 15 s. Only this spectrum has to be discarded in the further data analysis. The time "stamp" of any frequency spectrum is taken at half of the time duration of this spectrum, thus being 7.28 s for the first spectrum, with a time interval between two consecutive spectra of 14.4 s.
For a few number of injections (only in the second experiment) dedicated to the study of the short-lived $E^* = 1348.1(3)$ keV isomeric state of ^{207}Tl (see chapter 5), the parameters were the same compared with the ones used for the other injections, except the frame period which was reduced to 20 ms, giving a better time resolution in order to evaluate the decay of this isomeric state. In this case 25 consecutive frames have been averaged, leading to frequency spectra of 1.12 s duration each. The time "stamp" used for the decay rates evaluation is 0.56 s for the first frequency spectrum, and an time interval of 0.5 s for the following spectra.

3.1.3 Fourier analysis in the TCAP System

The TCAP system has provided an external FFT algorithm, which allows to set the FFT parameters "offline" and to optimize the analysis, depending on the purpose. It was modified to allow data merging in order to improve the frequency resolution of the spectra:

- The header of any block of the raw data is removed every $(r-1)$ block, where r is the resolution factor.
- The "new" data is obtained, with number of blocks divided by r, and number of samples per block multiplied by r, the observation time also multiplied by r.

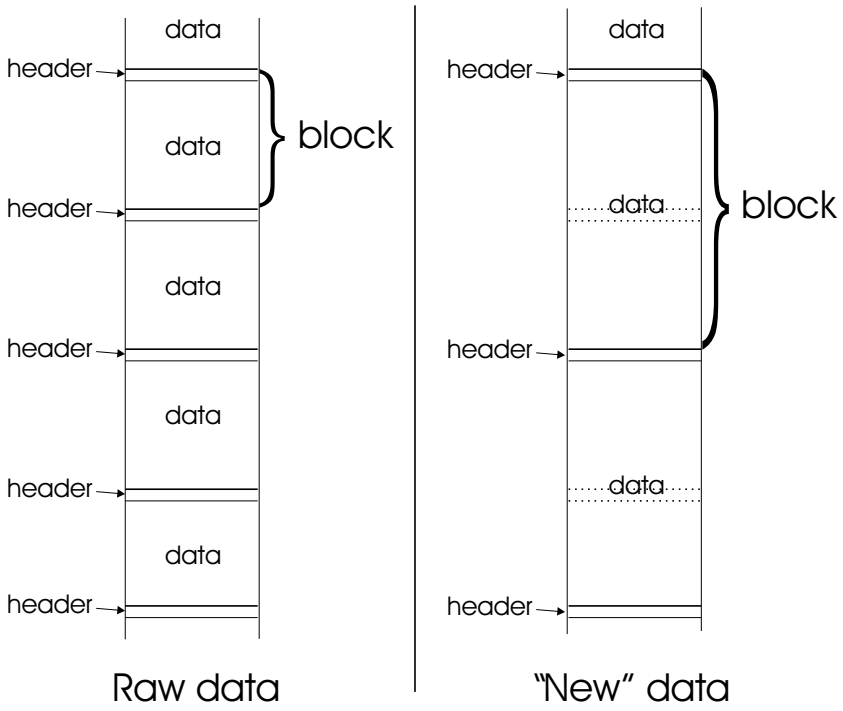

Figure 3.2: Principle of data merging. On the left part the raw data is shown. Every data block is structured with a header starting the block, giving information on the block acquisition (time, cooler parameters, ...), and 65536 (or 2^{16}) data samples following the header. On the right side, after the removal of one header every two blocks, the "new" data obtained has lower data block number, but increased number of samples per blocks and longer observation time, since the data flow corresponds to the time flow.

Figure 3.2 Increasing the number of samples per block will reduce as a consequence the width of any channel in the frequency spectra. This width δf is related to the observation time T_{obs} of any data block used by the FFT algorithm to produce the corresponding frequency spectrum, by the following equation:

$$\delta f = \frac{1}{T_{obs}} \tag{3.4}$$

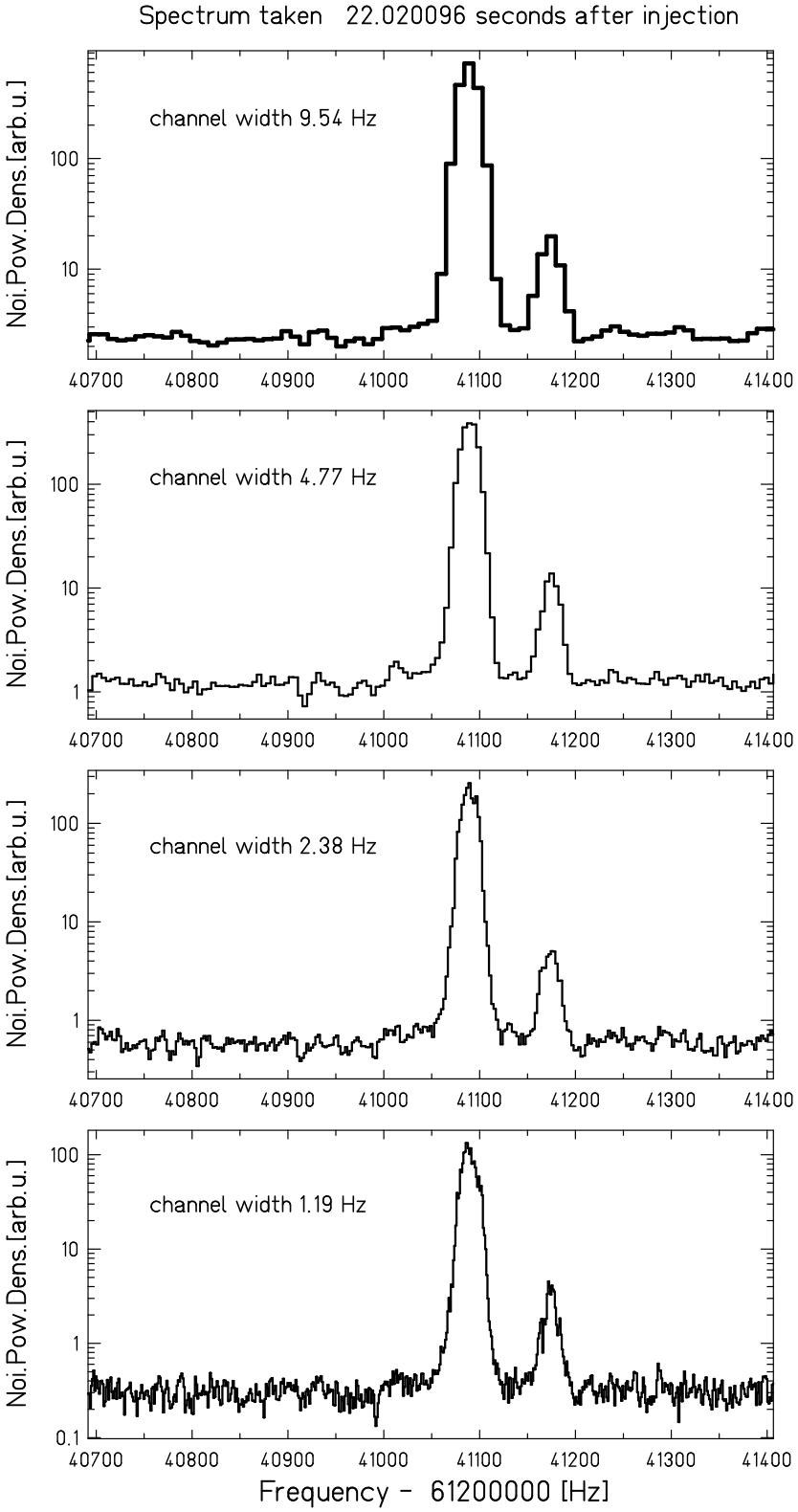

Figure 3.3: Comparison of frequency spectra produced from the same data, but with different resolution factors applied. From top to bottom, resolution factors 1, 2, 4, 8 have been used. Note that the background level decreases as the intensity is split into more channels. The left peak is $^{207}Tl^{81+}$, the right peak is $^{207}Pb^{81+}$.

The choice of the resolution factor must result from the compromise between the frequency resolution and the signal-to-noise ratio, the latter depending on the number of averages ($1/\sqrt{N_{aver}}$), as seen in equation 3.2). In order to create frequency spectra with a fixed time interval, the choice of different resolution factors will give different results, as shown in figure 3.3. The "real" number of averaged blocks will decrease as the resolution factor will increase, thus the background fluctuations as well as the frequency resolution will increase. Figure 3.3 shows that spectrum with resolution factor 1 has too poor frequency resolution, whereas spectrum with resolution factor 8 gives too high background fluctuations, and some artificial structure appear in the peaks (see the right peak). The choice of resolution factor 2 or 4 are a good compromise for the following processing of the data, resolution factor 4 (each frequency channel has a width of about 2.3842 Hz, corresponding approximately to a mass difference δm of about 42 keV in the vicinity of $^{207}Tl^{81+}$) was chosen to approach the same frequency resolution as in the SONY data .
As the intensity of the frequency bins after the FFT are very small (typical background intensity being $\approx 10^{-10}$ dBA), an arbitrary multiplication factor of 4×10^{12} was applied to these intensities. The factor 4 accounts for the fact that the application of a resolution factor leads to the splitting of the intensity between frequency channels. The parameters used for the FFT on the data from the second experiment were:

- Resolution factor 4
- Number of "real" averaged blocks 35
- Hanning Window

The Hanning window corresponds to a function:

$$w(k) = \frac{1}{2}\left[1 - cos\left(\frac{2\pi k}{N}\right)\right], \tag{3.5}$$

applied to the raw data, where N is the total number of samples per data block, and k the current sample number in the data block. The time duration of one block is determined by the ratio of the number of samples per block (here 65536) to the sampling frequency (here 640000 Hz), in this case it corresponds to 0.1048576 s. The averaging of (35×4) blocks leads to 14.680064 s duration spectra, with a time "stamp" at half of this duration.

3.2 Frequency spectra analysis

3.2.1 Principle

Each ion circulating in the ESR has a specific revolution frequency depending on its mass-over-charge ratio as seen in section 2.2. A peak is observed in the frequency spectra at this particular frequency. Analyzing the peak structure will give information on the ions of interest, in particular its mass-over-charge ratio and the number of particles. The mean value of the frequency distribution of any peak is directly related to the mass-over-charge ratio of the corresponding ions,

see equation 2.5. Thus a mass determination can be performed for all these ions, as it has already been done in past years [62, 59].

The area of the frequency distribution of any peak is proportional to the square of the electric charge of the corresponding ions, and to their number, as A $\propto$ N$\cdot$q^2 [52]. Since ^{207}Tl and ^{207}Pb have the same charge-state, e.g. 81$^+$, the area calibration will be the same for all peaks. The distribution of the frequency peaks is assumed to be gaussian. Also the fact that beyond some limit in the number of particles, the momentum distribution of the ions becomes dependent on the number of ions [51] as Δp/p $\propto$ N$^{1/3}$, could lead to a broadening of the two peaks, creating difficulties to resolve these peaks. It was taken into consideration by keeping the number of ^{207}Tl^{81+} ions injected into the ESR below 2000 particles.

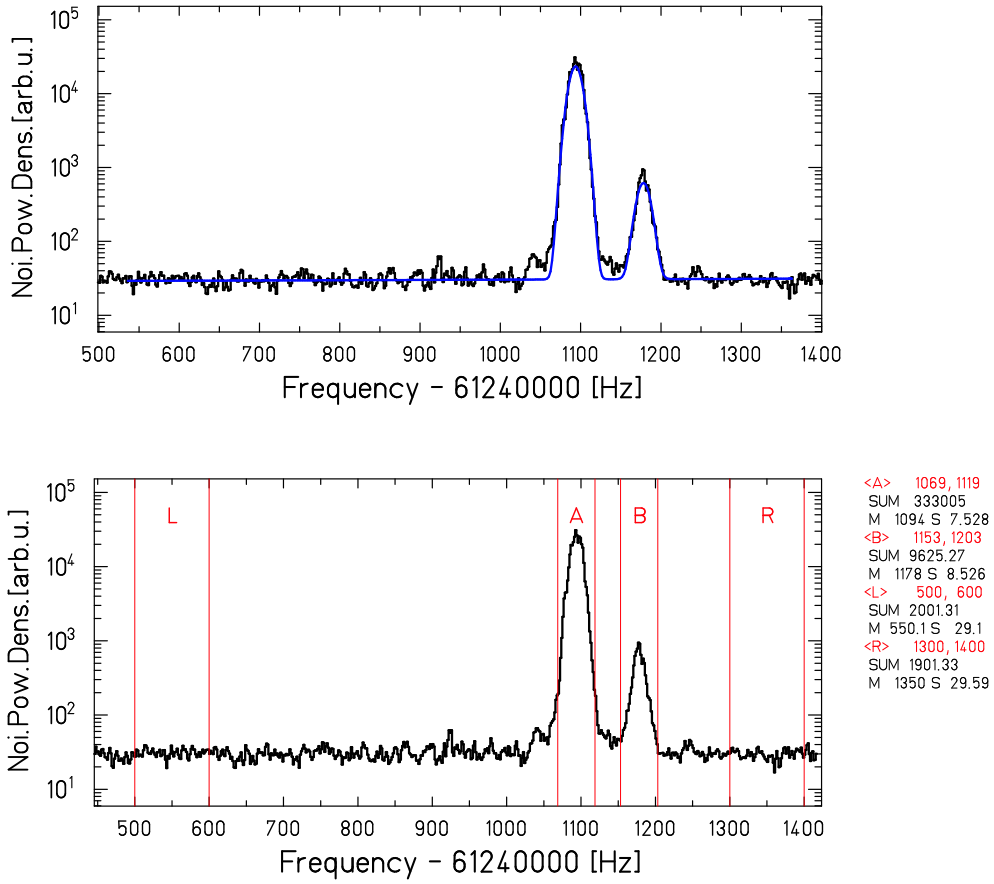

Figure 3.4: Example of analysis procedure on one spectrum from the SONY 3066 Spectrum Analyzer. Top: first-order polynomial fit to the background + 2 separate gaussian functions for the peaks. Note that the vertical scale is logarithmic. Therefore the tails observed, showing the continuing cooling process, are negligible. Bottom: integration of the background (L,R) for a fixed window of 100 Hz, and of the peaks (A = ^{207}Tl^{81+}, B = ^{207}Pb^{81+}) over a window defined from the fit results as [μ - 3σ, μ + 3σ], the limits are displayed in red colour.

3.2.2 Frequency spectra analysis in the SONY Spectrum Analyzer

The set of frequency spectra has been analyzed with the SATAN/GRAF software package [63]. The whole spectrum (bandwidth 1 kHz) is fitted with a first order polynomial function for the background. The error of the frequency bins is derived from equation 3.2. The result of this fit is kept as a baseline for the peak fits. Since the two peaks of interest ($^{207}Tl^{81+}$ and $^{207}Pb^{81+}$) are well resolved ($\Delta f \approx$ 85.4 Hz, see figure 4.1) each of them was fitted separately. A gaussian function was assumed for the peaks distribution, from the results of least-square fits to several peaks. The error of the frequency bins have been set to the square-root of the bins. The first moments of the distribution, the mean value μ and the standard deviation σ, are used for the integration method, where the channel intensities in the region of the peaks are summed over a window defined as [μ - 3σ, $\mu + 3\sigma$], which includes 99 % of the distribution of the peak. The background contribution to these sums is evaluated by summing the channel intensities over an arbitrary window of 100 Hz, on the left side and on the right side of the peaks, and subtracting the average value from the peak areas. Figure 3.4 displays the fit and integration results for one frequency spectrum.

An example of the evolution of all the parameters of the frequency distributions with time is shown in figure 3.5. One can see in figure 3.5-a) that the peaks have some drifts with time, which might occur due to the instability of the magnet power supplies. This drift is relatively small ($\delta f/f < \pm$ 100/61240000 $\sim \pm$ 1.6 $\times 10^{-6}$). Since all frequencies are shifting in parallel, the frequency difference between two peaks is stable, as seen in figure 3.5-d) and figure 4.1). This gives a justification to the use of the formula 2.5 to derive nuclear masses, as performed in refs. [62, 59]. The information relevant for the present analysis is the area of the distributions. The areas determined by the gaussian fit and the integration method have been compared. The relative deviation is smaller than 10 % on average, and cases where the deviation is beyond this level are explained by the fact that there was a large drift in frequency during the acquisition time of the blocks used by the FFT to produce the corresponding spectrum. Therefore the peak distribution was broadened artificially (not gaussian anymore), and the fit misestimated the peak areas, whereas the integration was not affected, because it relies more on the mean value of the peak from the fit (less affected by the broadening of the peak). For the determination of the decay rates the areas obtained by the integration method were exclusively used. Figure 3.5-c) shows that the width of the peaks is relatively stable during the measurement time, which means that the cooling process is practically finished after the acquisition time of the first spectrum of any injection. Only this one will be discarded for the analysis (also due to the decay of the isomeric state of ^{207}Tl).

3.2.3 Frequency spectra analysis in the TCAP System

With the frequency resolution of about 2.38 Hz, and a bandwidth of 312500 Hz, each spectrum has 131072 (2^{17}) data points. It corresponds to a file of about 2 Mb in size. To facilitate the further analysis, a frequency band of 10 kHz around the peaks of interest has been selected. The data obtained has also been analyzed with the SATAN/GRAF software package [63]. The background was fitted with

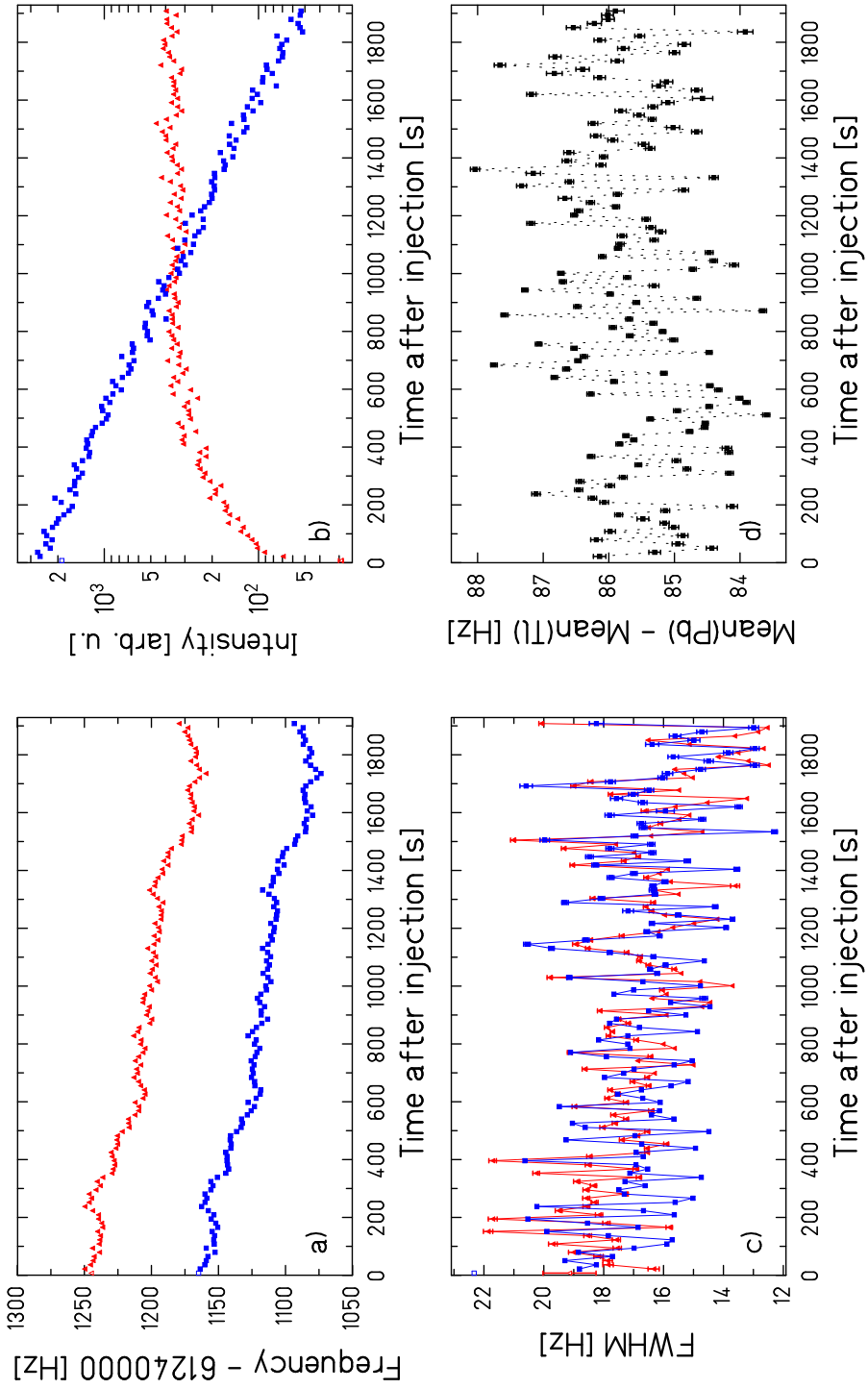

Figure 3.5: Evolution of the results of the frequency peaks analysis of $^{207}Tl^{81+}$ and $^{207}Pb^{81+}$ with time, for one injection. Results are displayed in blue squares for $^{207}Tl^{81+}$, in red triangles for $^{207}Pb^{81+}$. a) mean frequency of the distributions, b) peak areas (equation 3.8 has been used to fit the blue curve, equation 3.9 the red curve), c) width of the peaks (FWHM), d) difference between the mean frequencies of $^{207}Pb^{81+}$ and $^{207}Tl^{81+}$ (indirectly determined from the figure a) results).

a 1st order polynomial function. The further procedure is the same as described in section 3.2.2. The peak areas obtained from the integration method were also kept for the decay rates evaluation.

3.3 Decay rates determination

The areas of the frequency distribution of $^{207}Tl^{81+}$ and $^{207}Pb^{81+}$ have been obtained from the frequency spectra analysis at different times after the injection into the ESR. Therefore, from the evolution of these areas with time, the decay constant of these ions and the initial number of ions injected into the ESR can be derived. In the following, $N_{Tl}(t)$ and $N_{Pb}(t)$ represent the number of $^{207}Tl^{81+}$ and $^{207}Pb^{81+}$ ions at time t, respectively. $\lambda_{tot}^{Tl,Pb}$ is the total decay constant for these ions, accounting for nuclear and non-nuclear "losses" ($^{207}Pb^{81+}$ is a stable ion, therefore there is no nuclear decay). λ_{β_b} and λ_{β_c} are the decay constants for the bound-state and continuum-state β-decay of $^{207}Tl^{81+}$, respectively. λ_{loss} is the decay constant for the non-nuclear processes. The equations describing the evolutions of $^{207}Tl^{81+}$ and $^{207}Pb^{81+}$ ions with time are the following:

$$\frac{dN_{Tl}(t)}{dt} = -\lambda_{tot}^{Tl} N_{Tl}(t), \tag{3.6}$$

$$\frac{dN_{Pb}(t)}{dt} = -\lambda_{tot}^{Pb} N_{Pb}(t) + \lambda_{\beta_b} N_{Tl}(t). \tag{3.7}$$

The total decay constants for $^{207}Tl^{81+}$ and $^{207}Pb^{81+}$ are:

$$\lambda_{tot}^{Tl} = \lambda_{\beta_b} + \lambda_{\beta_c} + \lambda_{loss}^{Tl}, \tag{3.8}$$

$$\lambda_{tot}^{Pb} = \lambda_{loss}^{Pb}. \tag{3.9}$$

The non-nuclear "losses" are mainly due to radiative electron capture from the electron cooler, to interaction with the residual gas remaining in the storage ring and to electron loss of partially-ionized atoms. This depends mainly on the number of bound electrons to any ion and of the atomic number of this ion. Thus each ion circulating in the ring has a characteristic "loss" decay constant. The two ions of interest ($^{207}Tl^{81+}$ and $^{207}Pb^{81+}$) have unoccupied orbit(s) in the K electronic shell and very similar atomic number ($\Delta Z/Z \approx 1.2$ %). Previous experiments showed that the non-nuclear "losses" are nearly equal for bare and hydrogen-like isobars. The assumption that $\lambda_{loss}^{Pb} \approx \lambda_{loss}^{Tl} \approx \lambda_{loss}$ will be made for the following analysis. λ_{tot}^{Pb} will be replaced by λ_{loss}, and λ_{tot}^{Tl} by λ_{tot}. The solution of the differential equation 3.6 is:

$$N_{Tl}(t) = N_{Tl}(0) e^{-\lambda_{tot} t}. \tag{3.10}$$

The solution of the differential equation 3.7 is the sum of two components, the solution without second member, similar to equation 3.10, and the solution with second member, which is derived using the "constant variation" method. Assuming a solution on the form:

$$N_{Pb}(t) = F(t) e^{-\lambda_{loss} t}, \tag{3.11}$$

the derivative is:

$$\frac{dN_{Pb}(t)}{dt} = -\lambda_{loss}F(t)e^{-\lambda_{loss}t} + F'(t)e^{-\lambda_{loss}t}. \quad (3.12)$$

By replacing the terms of equation 3.7 by the ones obtained in equations 3.10, 3.11 and 3.12, one derives:

$$F'(t) = N_{Tl}(0)\lambda_{\beta_b}e^{(\lambda_{loss}-\lambda_{tot})t}, F(t) = N_{Tl}(0)\frac{\lambda_{\beta_b}}{\lambda_{loss}-\lambda_{tot}}e^{(\lambda_{loss}-\lambda_{tot})t} + C. \quad (3.13)$$

The constant C is determined from the value F(t=0) = 0 as:

$$C = N_{Tl}(0)\frac{\lambda_{\beta_b}}{\lambda_{tot}-\lambda_{loss}}. \quad (3.14)$$

Using equations 3.11, 3.13 and 3.14, the total solution of equation 3.11:

$$N_{Pb}(t) = N_{Pb}(0)e^{-\lambda_{loss}t} + N_{Tl}(0)\frac{\lambda_{\beta_b}}{\lambda_{tot}-\lambda_{loss}}(e^{-\lambda_{loss}t} - e^{-\lambda_{tot}t}). \quad (3.15)$$

Equations 3.10 and 3.15 have been used as fit functions for the area evolution curves of $^{207}Tl^{81+}$ and $^{207}Pb^{81+}$ respectively. One example is shown in figure 3.5-b). The first spectrum of each injection, recorded right after the injection of the ions in the ESR, has not been used for the analysis, because it includes the cooling process (about 7 s) and the decay of the isomeric state of $^{207}Tl^{81+}$. The latter isomeric state is completely decayed after about 15 s. As mentioned in section 3.2.1, the peak areas in the frequency spectra are proportional to the corresponding number of particles stored in the ring. The fact that the $^{207}Tl^{81+}$ and $^{207}Pb^{81+}$ ions have the same calibration factor means that the derivation of all the fit parameters from the previous equations is independent of the absolute areas of the peaks. Therefore it is not needed to include a calibration factor of the peak areas into these equations.
The errors of the areas determined with the integration method were determined from two contributions, first the statistical error defined as:

$$\sigma_{stat}(A_i^{data}) = \sqrt{\left|A_i^{data} - A_{i-1}^{data}\right|}. \quad (3.16)$$

This was determined by analogy to the particle counting method where the measured variable is the number of particles emitted from the decay of any nuclide in a given time interval. This corresponds to the number of mother nuclides that have decayed in this time interval. Therefore the *variation* of intensity with time, directly related to the variation of corresponding particles in time, is the statistical variable.
The areas provided by the FFT algorithm show large fluctuations, even where they are supposed to be almost constant. A good example is the "flat" part of the area evolution curve of $^{207}Pb^{81+}$ as shown in figure 3.5-b). The second error contribution, the systematical error, is defined from this observation as relative to the areas:

$$\frac{\sigma_{syst}(A_i^{data})}{A_i^{data}} = \frac{\sigma(\bar{A}^{data}(Pb))}{\bar{A}^{data}(Pb)}, \quad (3.17)$$

where A_i^{data} and A_i^{fit} are respectively the peak areas obtained from the data (peak areas fit) and for the decay curves fit in the spectrum with index i, either for $^{207}Tl^{81+}$ or $^{207}Pb^{81+}$. The quantities $\bar{A}^{data}$(Pb) and $\sigma(\bar{A}^{data}(\mathrm{Pb}))$ are the mean value and the standard deviation of the $^{207}Pb^{81+}$ data points, in a region defined by the fit results as:

$$\frac{\left|A_i^{fit}(Pb) - A_{i-1}^{fit}(Pb)\right|}{A_{i-1}^{fit}(Pb)} \leq 4.3 \times 10^{-2} \cdot N_{av}, \tag{3.18}$$

where N_{av} is the number of blocks averaged for the FFT. The region defined as above corresponds to the "plateau" region of the $^{207}Pb^{81+}$ area evolution curve, where the non-nuclear losses and the feeding from the bound-state β-decay of $^{207}Tl^{81+}$ are in equilibrium (see figure 3.5-b). In this region the intensity of the frequency peaks is supposed to be stable, therefore the relative deviation from an average value corresponds to the relative systematical error of this value. The region definition was determined from the criterion $\left|A_i^{fit}(Pb) - A_{i-1}^{fit}(Pb)\right|/A_{i-1}^{fit}(\mathrm{Pb}) \leq 1.5\times10^{-3}$ for 35 averages.
These two errors are quadratically added to derive the total error. Since the systematical errors are related to the results, a recursive procedure is necessary for the fits. The error calculation iterations were performed as the following:

1. A first estimation of the error bars is done
2. A fit is performed using equation 3.10 to the Tl decay curve.
3. A fit is performed, using equation 3.15 and the results from step 3., to the Pb decay curve.
4. From the fit results new systematical errors are calculated.
5. Back to step 2.

If at step 4. the region defined for the systematical error calculations is not changed by the fit results, the iteration stops. The fits are performed consecutively and independently, this means first the Tl curve is fitted with equation 3.10, and then the Pb curve with equation 3.15, using the results from the Tl curve as fixed parameters. The χ^2 obtained from the fits using these errors as defined above do not show a systematical deviation from the expected values.

Chapter 4

Results and comparison with calculations

4.1 Results

For each injection the decay constants λ_{tot}^{Tl}, λ_{β_b} and λ_{loss} (see section 3.3 for definition of these parameters) have been obtained, and λ_{β_c} can be derived from equation 3.8. Therefore the total nuclear decay constant of $^{207}Tl^{81+}$ λ_{nuc}^{Tl} defined as:

$$\lambda_{nuc}^{Tl} = \lambda_{\beta_b} + \lambda_{\beta_c} = \lambda_{tot}^{Tl} - \lambda_{loss}, \tag{4.1}$$

can also be derived. The two main results obtained in both experiments, the total nuclear half-life of $^{207}Tl^{81+}$ and the branching ratio of the bound-state β-decay process in this nuclide, will be discussed and compared with calculations.

4.1.1 First experiment with $^{207}Tl^{81+}$ fragments

The derivation of results from the first experiment which studied the bound-state β-decay of $^{207}Tl^{81+}$ have been described in ref. [57]. In principle the description of this derivation is similar to section 4.1.2. The only main difference is that the decay constant λ_{loss}, accounting for the non-nuclear losses happening to the ions in the ESR, has been determined from the "decay" of stable $^{207}Pb^{81+}$ after the complete vanishing of $^{207}Tl^{81+}$ ions, in some long injections (about 4000 s duration). The results obtained in the rest frame are:

- λ_{tot}^{Tl} (rest frame) = 3.26(6) $\times$ 10^{-3} s^{-1}
- λ_{β_b} (rest frame) = 0.429(29) $\times$ 10^{-3} s^{-1}
- λ_{loss} (rest frame) = 0.543(10) $\times$ 10^{-3} s^{-1}.
- λ_{β_c} (rest frame) = 2.29(12) $\times$ 10^{-3} s^{-1}

The total nuclear decay constant of $^{207}Tl^{81+}$ is derived from these results using equation 4.1:

$$\lambda_{nucl}^{Tl} \text{ (rest frame)} = 2.72(12) \times 10^{-3} \text{ s}^{-1},$$

and the half-life is:

$$T_{1/2}^{Tl}(experiment) = 255(11)s. \tag{4.2}$$

The branching ratio of the bound-state β-decay of $^{207}Tl^{81+}$ is deduced:

$$\frac{\lambda_{\beta_b}}{\lambda_{nucl}^{Tl}}(experiment) = 0.157(13). \tag{4.3}$$

The comparison of these results with the ones from the second experiment is presented in the next section, where they are also compared with predictions and calculations.

4.1.2 Second experiment with $^{207}Tl^{81+}$

From the files recorded during the second experiment, a slightly different set was available from the two different recording systems, due to some differences in the data acquisition procedure (see section 2.3.4). The list of the results obtained from the SONY and TCAP systems for each individual injection is presented in appendixes A and B, respectively. The distributions of the fit parameters λ_{tot}^{Tl}, λ_{β_b} and λ_{loss} are displayed also in the appendixes, in figures A.1 to A.6 for SONY data, and figures B.1 to B.6 for TCAP data. Also the distribution of the frequency difference between $^{207}Tl^{81+}$ and $^{207}Pb^{81+}$ is shown in figure 4.1, only for SONY data. The average value obtained for the decay constants (in the laboratory frame) are obtained from 48 files recorded by the SONY spectrum analyzer, and 43 files recorded by the TCAP system:

- λ_{tot}^{Tl} (lab. frame) = 2.080(71) $\times$ 10^{-3} s^{-1}
- λ_{β_b} (lab. frame) = 0.306(29) $\times$ 10^{-3} s^{-1}
- λ_{loss} (lab. frame) = 0.182(55) $\times$ 10^{-3} s^{-1}
- λ_{β_c} (lab. frame) = 1.592(94) $\times$ 10^{-3} s^{-1}

for SONY data, and:

- λ_{tot}^{Tl} (lab. frame) = 2.077(81) $\times$ 10^{-3} s^{-1}
- λ_{β_b} (lab. frame) = 0.311(29) $\times$ 10^{-3} s^{-1}
- λ_{loss} (lab. frame) = 0.187(57) $\times$ 10^{-3} s^{-1}
- λ_{β_c} (lab. frame) = 1.579(103) $\times$ 10^{-3} s^{-1}

for TCAP data. The results derived from the two different datasets are in excellent agreement with each other. The SONY data available includes more injections than the TCAP data available, and therefore will be used for the following. All the decay constants have been obtained in the laboratory frame. To convert them to the center of mass frame (or rest frame), as λ (rest frame) = $\gamma \cdot \lambda$ (lab. frame), it is needed to calculate the Lorentz factor γ. To determine it, the following formula is derived from $E_e^{kin} = m_e c^2 (\gamma - 1) = e \cdot U_{cooler}$ as:

$$\gamma = 1 + \frac{e \cdot U_{cooler}}{m_e c^2} \tag{4.4}$$

where e is the elementary charge, m_e is the electron mass, c the speed of light, U_{cooler} the nominal value of the electron cooler high voltage. The latter value must be corrected from space-charge effects depending on the electron cooler current I_{cooler} by using the following relation:

$$U_{cooler}^{eff} = U_{cooler} - \frac{C \cdot I_{cooler}}{\sqrt{1-\gamma^{-2}}}, \tag{4.5}$$

where C = 113 V $\cdot$ A^{-1}. A new value of the Lorentz factor is deduced with equation 4.4 by replacing U_{cooler} by the effective cooler voltage U_{cooler}^{eff}. With the settings used for the experiment (U_{cooler} = 220020 V, I_{cooler} = 100 mA, see section 4.1.2), a value of $\gamma^{eff} = 1.430537$ is obtained. The relative error of this value is less than 5×10^{-6} and can be neglected for the following calculations. The corrected values of the decay constants in the rest frame are:

- λ_{tot}^{Tl} (rest frame) = 2.976(102) $\times$ 10^{-3} s^{-1}
- λ_{β_b} (rest frame) = 0.438(41) $\times$ 10^{-3} s^{-1}
- λ_{loss} (rest frame) = 0.260(79) $\times$ 10^{-3} s^{-1}
- λ_{β_c} (rest frame) = 2.278(135) $\times$ 10^{-3} s^{-1}

There is some difference between these results and the ones obtained in the first experiment presented in section 4.1.1. The main difference comes from the non-nuclear losses decay constant. The difference shows that the beam lifetime has been improved from about 20 min to about 45 min. This difference is appearing also in the total decay constant, which by definition includes the non-nuclear losses. The nuclear decay constants λ_{β_b} and λ_{β_c} are similar. When "experimental results" will be quoted in the following, they will exclusively refer to the ones of the second experiment and from SONY data. From these values and equation 4.1, the nuclear decay constant of $^{207}Tl^{81+}$ is derived as:

$$\lambda_{nucl}^{Tl} \text{ (rest frame)} = 2.716(129) \times 10^{-3} \text{ s}^{-1},$$

and its half-life is:

$$T_{1/2}^{Tl}(experiment) = 255(12)s. \tag{4.6}$$

The half-life obtained for fully-ionized $^{207}Tl^{81+}$ is reduced by about 11 % compared with the half-life of 286(2) s for the neutral atom measured by Trischuk and Kankeleit [53]. This can be explained by three effects: The removal of the electrons which modifies the Fermi function F(Z,E), the change in the Q-value due to the difference in the total binding energies of the electrons in the mother and daughter nuclides, and the opening of an additional decay mode, the bound-state β-decay. The two first effects apply to the continuum-state β-decay process. The partial half-life obtained for the continuum-state β-decay of $^{207}Tl^{81+}$ is determined from the results obtained as:

$$T_{1/2}^{Tl}(\beta_c) \text{ (experiment)} = 304(18) \text{ s},$$

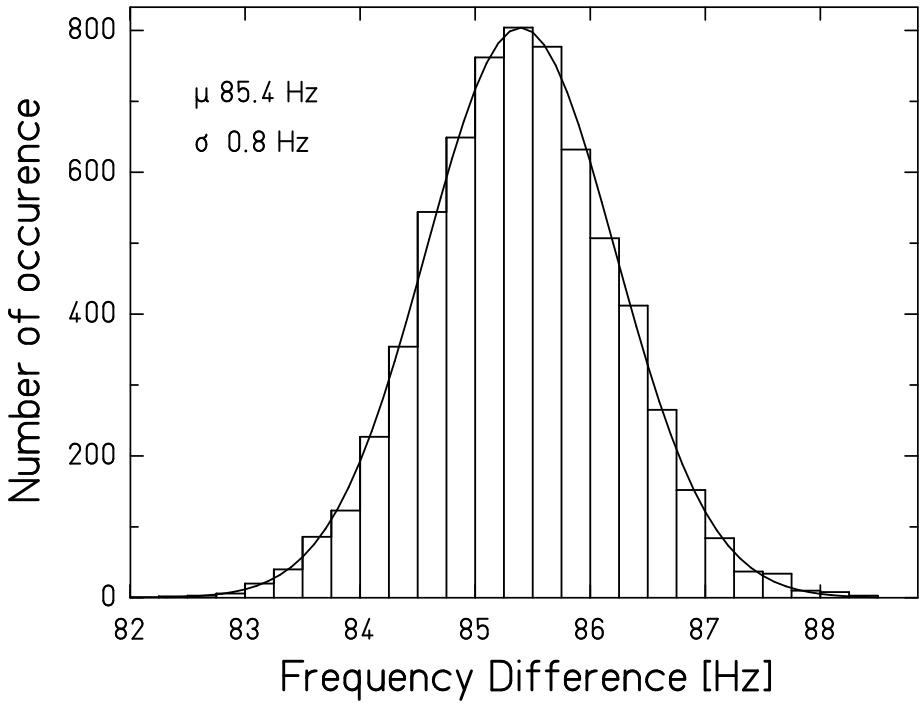

Figure 4.1: Distribution of the frequency difference between the mean values of $^{207}Pb^{81+}$ and $^{207}Tl^{81+}$ peaks in all the frequency spectra, from the second experiment and SONY data.

which is increased by about 6 % compared to the value for the neutral atom. The screening effect for this transition is deduced from atomic data tables [54] as a factor of about 1.025 to be mupltiplied with the Fermi function for the main transition of the $^{207}Tl^{81+}$ β-decay going to the ground-state of $^{207}Pb^{81+}$, and about 1.036 for the small branch going to an excited state of $^{207}Pb^{81+}$. Using the known branchings of the β^--decay of the neutral atom of ^{207}Tl [55] displayed in figure 4.2, the total decrease of the half-life due to the vanishing of the screening is about 2.5 %. The removal of the bound electrons also change the mass difference between $^{207}Tl^{81+}$ and $^{207}Pb^{81+}$ due to the differences in binding energies of the electrons for the mother and daughter atoms. This difference has been evaluated as 17 keV [25], thus the Q-value of the transitions will be reduced by this amount. With the estimated dependence on the decay rate with the fifth power of the Q-value, the half-life will be increased by about 4.5 %. The overall effects resulting from the electron stripping are expected to lead to an increase in the continuum-state β-decay half-life of ^{207}Tl by about 2 %, a result slighty smaller than the experimental result. Table 4.1 summarizes these observations.

The other important result derived from the decay rates estimation is the respective branchings of bound-state and continuum-state β-decay in $^{207}Tl^{81+}$. The branching ratio of the bound-state β-decay is obtained as:

$$\frac{\lambda_b}{\lambda_{nucl}^{Tl}}(experiment) = 0.161(17). \tag{4.7}$$

Calculated		Experimental
Screening	Q-value	
-2.5 %	+4.5 %	
+2 %		+6 %

Table 4.1: Summary of the calculated and observed modification in the half-life of the continuum-state β-decay of $^{207}Tl^{81+}$, compared to the half-life of $^{207}Tl^{0}$.

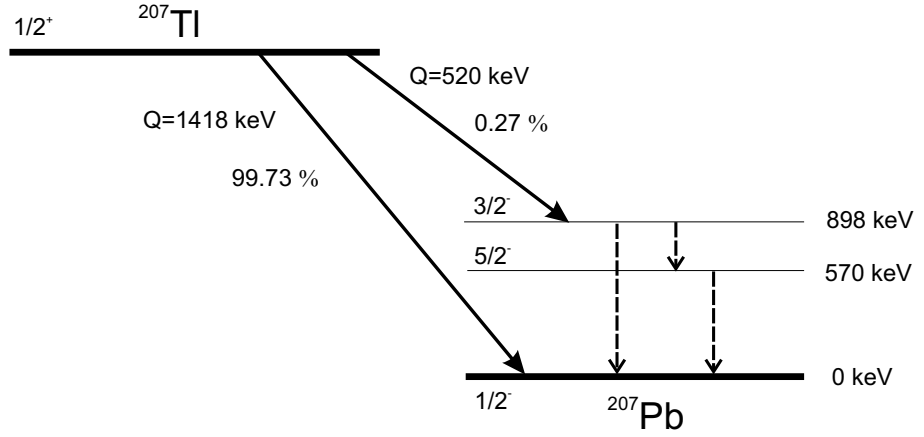

Figure 4.2: Decay scheme of the ground state of ^{207}Tl, taken from ref. [55].

The mean frequency difference between the $^{207}Pb^{81+}$ and $^{207}Tl^{81+}$ peaks in the frequency spectra has been obtained as 85.4(8) Hz, the distribution of this result is shown in figure 4.1. A similar result for the mean frequency difference between the isomeric and ground states of $^{207}Tl^{81+}$ has been derived (from the analysis described in chapter 5), as 76.1(2.9) Hz. Using these two results and the known excitation energy of the isomeric state of ^{207}Tl [55], which is not affected by the electron stripping, by scaling this energy difference with the frequency differences, the Q-value for the bound-state β-decay of $^{207}Tl^{81+}$ can be derived as:

$$Q_{\beta_b^-}^{q=Z}(experiment) = 1513(59)keV. \tag{4.8}$$

This Q-value correspond to the bound-state β-decay with the electron going into the K shell, which accounts for about 80 % of the total bound-state β-decay. The expected Q-value for the bound-state β-decay of $^{207}Tl^{81+}$ is derived from the Q-value of the neutral atom [27] using equations 1.22 and 1.23:

$$Q_{\beta_b^-}^{q=Z}(theory) = 1502(5)keV, \tag{4.9}$$

which is in very good agreement with the experimental result.

4.2 Decay rates calculations

To test the experimental results obtained for the decay rates of bound-state and continuum-state β-decay of $^{207}Tl^{81+}$, calculations based on refs. [33, 39] were performed. The basic relations necessary to perform the calculations are equations 1.10 and 1.20. Either the ratio λ_b/λ_c or the absolute decay rates can be

computed. The assumption that the electron energy spectrum for the continuum-state β-decay is following the allowed shape, if experimental data has proved it, will be used for all the following.

4.2.1 Bound-to-continuum ratio

From equations 1.10 and 1.19, the ratio λ_b/λ_c is:

$$\frac{\lambda_b}{\lambda_c} \propto \frac{\left|M_{fi}^{bound}\right|^2 \sum_x \sigma_x \left[max(\psi_f, \psi_g)\right]^2 E_{\bar{\nu}_e}^2}{\left|M_{fi}^{cont}\right|^2 f(Z,E)}. \tag{4.10}$$

By considering that the two decay modes involve the same transition between two nuclear states, one can replace both matrix elements by the same effective matrix element $\left|M_{fi}^{eff}\right|$. Therefore they will cancel in equation 4.10 and show that the calculation of the relative branchings of the bound-state and continuum-state β-decay are independent of the transition type. Equation 4.10 becomes:

$$\frac{\lambda_b}{\lambda_c} \propto \frac{\sum_x \sigma_x \cdot \left[max(\psi_f, \psi_g)\right]^2 \cdot E_{\bar{\nu}_e}^2}{f(Z,E)}. \tag{4.11}$$

This ratio can be computed for any (Z, E) combination. Only the cases where transitions are energetically possible for both bound-state and continuum-state β-decay (there is a difference in Q-value due to the binding energy of the electron in a bound state) can be predicted with such formula. The result of the calculations performed for mother nuclides, with Z_i ranging from 10 to 90, and released energy E from 20 keV to 5 MeV, have been already displayed in figure 1.3. It has to be noted that this calculation is valid only for a given transition between two nuclear states. The branching ratio $\lambda_b/(\lambda_b+\lambda_c)$ is easily derived from λ_b/λ_c as:

$$\frac{\lambda_b}{\lambda_b + \lambda_c} = \frac{1}{1 + \left(\frac{\lambda_b}{\lambda_c}\right)^{-1}} \tag{4.12}$$

In the case of a β-unstable nuclide which decays to different levels of the daughter nuclide, to get a realistic calculation for the total branching ratio of the bound-state β-decay process, one has to weight the results obtained for each individual transition with the branching of this transition. In the case of ^{207}Tl, two transitions mainly exist. The calculations give that the transition to the ground state of ^{207}Pb has a bound-state β-decay branching ratio of 14.65 %, and that the transition to the 898 keV excited level of ^{207}Pb has a branching of 48.88 %. Using these numbers and the branchings of each transition for ^{207}Tl as a neutral atom [55] shown in figure 4.2, the average branching ratio for the bound-state β-decay is:

$$\frac{\lambda_b}{\lambda_b + \lambda_c}(theory) = 0.146(1), \tag{4.13}$$

and is in very good agreement with the experimental observations of 0.161(17). The comparison of the branching ratio of bound-state β-decay between the result obtained from the second experiment on $^{207}Tl^{81+}$ and calculations for $Z_i = 81$ (Tl isotopes) is shown in figure 4.3. Other experimental information on the bound-state β-decay branching, for instance on other Tl isotopes , is necessary to give a better estimate on the reliability of the calculations.

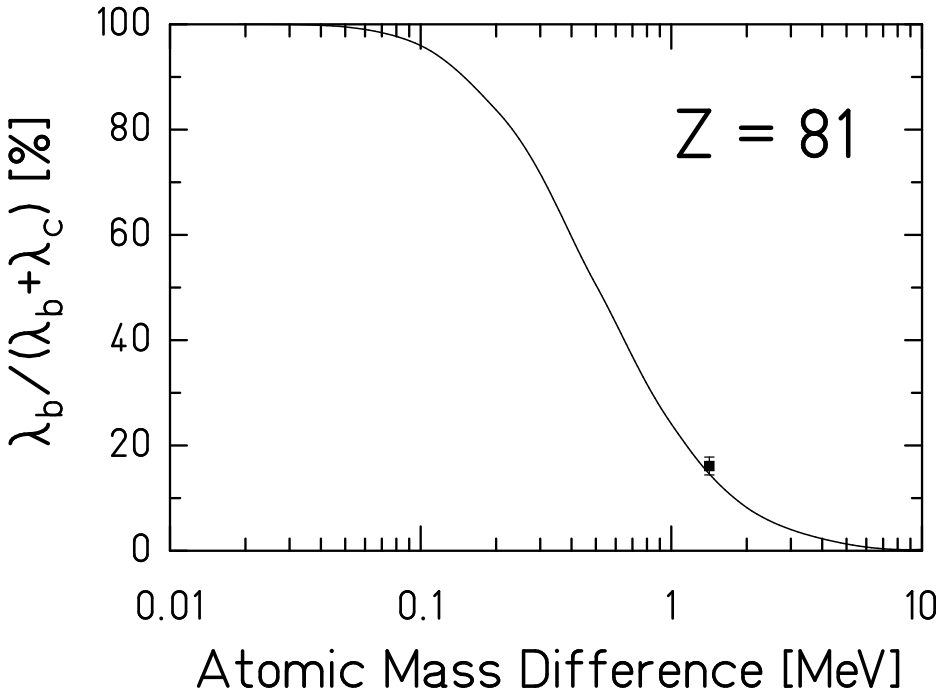

Figure 4.3: Comparison between the experimental branching ratio of bound-state β-decay in $^{207}Tl^{81+}$ (black square) and calculations for Z=81 isotopes (solid line).

4.2.2 Absolute decay rates

To derive the absolute decay rates of a transition without having to calculate the matrix element involved into this transition, the experimental results known from the neutral atom can be used. The assumption that the *ft*-value is not modified by the electron stripping is made, which allows, by performing the calculation of the f function for the fully-ionized atom, to derive its half-life by using the "neutral" *ft*-value. The decay rate of a fully-ionized atom can be expressed as:

$$\lambda^* = \frac{ln2 \cdot f^*}{f^0 \cdot t_{1/2}}, \tag{4.14}$$

where f^0 and f^* are the f-functions for the neutral and fully-ionized atom, respectively, $t_{1/2}$ is the partial half-life for the given transition (in the case of a neutral atom). Such relation can be also computed for any energetically possible transition. It has to be for a nuclide as a neutral atom *and* as a fully-ionized atom. In the case of ^{187}Re seen in section 1.6.2, the transition to the 9.746 keV excited state of ^{187}Os is only possible if ^{187}Re is stripped from most of its electrons. In such case a $log(ft)$-value derived from systematics has to be used, as authors of ref. [33] had to deal with, in order to predict the half-life of $^{187}Re^{75+}$. The input parameters needed to perform a calculation are the mother nuclide's mass number, atomic number, number of bound electrons, the Q-value for the β-decay (as a neutral atom), the β-decay half-life, the populated levels of the daughter nuclide (including the branching of each level), the spin and parities of

all levels involved in the transitions. The output given are the bound-state and continuum-state β-decay rates for each transition weighted with the branching of this transition. The sum of individual decay rates for each transition gives the total decay rate of this process. For $^{207}Tl^{81+}$ the input is obtained from refs. [27, 55], which leads to total bound-state and continuum-state β-decay rates as:

$$\lambda_b(theory) = 0.406(2) \times 10^{-3} s^{-1} \tag{4.15}$$

$$\lambda_c(theory) = 2.37(2) \times 10^{-3} s^{-1} \tag{4.16}$$

These results are in very good agreement with those obtained in the two experiments. This is particularly interesting for the continuum-state decay constant, which was indirectly determined in the experiments from three parameters. The predicted branching ratio of the bound-state β-decay process is exactly the same as calculated with the method described in section 4.2.1. The expected total nuclear half-life of $^{207}Tl^{81+}$ can be derived from these calculations as:

$$T_{1/2}^{Tl}(theory) = 250(3)\ s. \tag{4.17}$$

For this value experimental results and calculation are also in very good agreement. This shows the feasibility of predicting decay rates for fully-ionized nuclides. Restrictions are set to the nuclides where all necessary spectroscopic information for the neutral atom is available (Q-value, half-life, spin, population of levels of daughter nuclide).

Chapter 5

Production and lifetime measurements of isomeric states

5.1 Half-life evaluation of the $^{207}Tl^{81+}$ isomeric state

As explained in section 3.1.2, some files were dedicated to the study of the 1348 keV isomeric state of ^{207}Tl. The given excitation energy requires a frequency resolution of f/Δ f $\sim 8 \times 10^5$ (corresponding to a mass resolution m/Δm $\approx$ 150000) to be able to resolve the peaks in a frequency spectrum, which is below the maximum achieved in past experiments [62, 59]. The literature half-life of this isomeric state is 1.33(11) s [55, 64]. Nuclides having a nuclear half-life below 10 s (except for highly-converted isomeric states, see ref. [9]) could not be observed with Schottky Mass Spectrometry (SMS) using only the electron cooler, because the reduction of the momentum spread by electron cooling has a rather long period, 30 s or more. The stochastic precooling system was not only applied to improve the evaluation of the bound-state β-decay constant, which depends strongly on the rising part of the $^{207}Pb^{81+}$ decay curve in the beginning of the measurement, but also to be able to observe this isomeric state and measure its decay constant.

The analysis of the dedicated files also allows to determine more precisely the cooling time resulting from the application of the stochastic precooling. From this time until the complete decay to the $^{207}Tl^{81+}$ isomeric state can be used to evaluate its half-life, therefore a range of 5 to 10 s is expected to be useful for the analysis. The injections lasted 20 s, and frequency spectra of 25 averages, 1.12 s duration and 0.5 s interval were created. The areas of the peaks were determined as in section 3.2.2. The two time-dependent curves have been fitted using equation 3.10:

$$N_{Tl}(t) = N_{Tl}(0)e^{-\lambda_{tot}t} \tag{5.1}$$

The fits of the ground and isomeric state of $^{207}Tl^{81+}$ areas evolutions with time are given in figure 5.1 for one run. Taking the average of the fit results from the three analyzed runs leads to:

$$\lambda(lab.frame) = 0.329(72)\ s^{-1}, \tag{5.2}$$

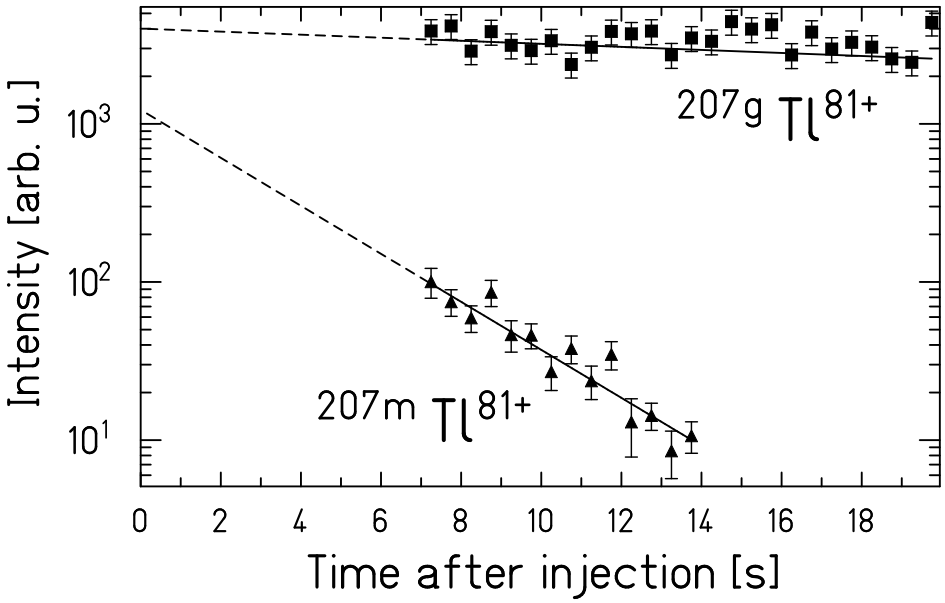

Figure 5.1: Time evolution of ground and isomeric states of $^{207}Tl^{81+}$ in one run. The solid lines correspond to the fit using equation 5.1, the dashed lines are extrapolation to t = 0.

in the laboratory frame. The non-nuclear losses decay constant can be neglected because its contributes to less than 0.1 % of the total decay constant, according to the results obtained for the ground state of $^{207}Tl^{81+}$ in the previous chapter. Using the same Lorentz factor $\gamma^{eff} = 1.430537$ as in section 4.1.2, the decay constant obtained is:

$$\lambda(restframe) = 0.471(102)\ s^{-1}, \tag{5.3}$$

and the half-life is:

$$T_{1/2}(experiment) = 1.47(32)\ s. \tag{5.4}$$

The value of the half-life is slightly different from the literature value, but this can be explained because the result of Eccleshall and Yates [64] was obtained with a neutral atom, whereas in this experiment the isomeric state, as an atom, was fully-ionized.

An isomeric transition is shared between two branches: γ emission and Internal Conversion (IC). The first branch is basically the emission of a photon with an energy corresponding to the energy difference between the two levels involved in the transition. If the photon is energetic enough ($E > 2 \cdot m_e c^2$), it can also transform into an electron-positron pair. The second branch involves the bound electrons, in the sense that the excitation energy of the nucleus is transmitted to one of these electrons, being emitted. Usually the more bound electrons from the K orbital are emitted, resulting in a rearrangement cascade and either X-ray photons or Auger electrons emission. To derive the decay constant of a fully-ionized atom from a neutral atom for an isomeric state, if it decays only via

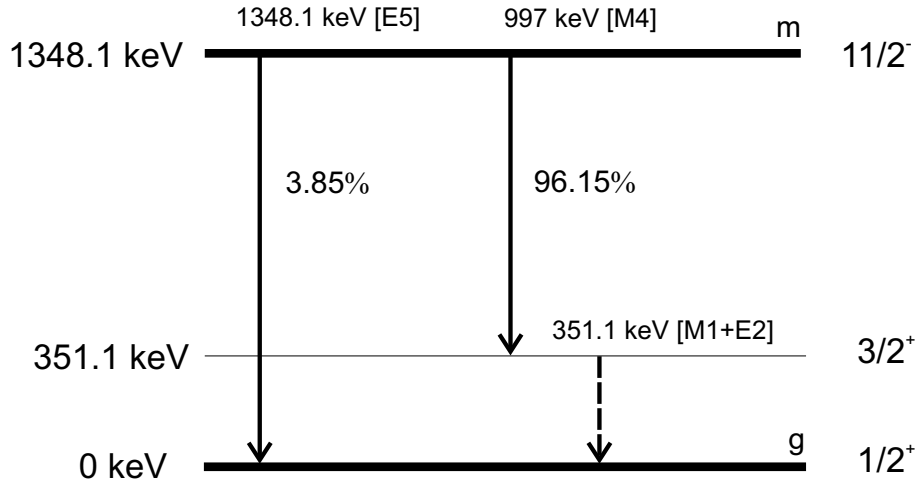

Figure 5.2: Decay scheme of the isomeric state of ^{207}Tl, taken from ref. [55]

isomeric transition, the following formulas are used:

$$\lambda_{IT}^{q=0} = \lambda_\gamma + \lambda_{IC}, \tag{5.5}$$

$$\lambda_{IT}^{q=Z} = \lambda_\gamma. \tag{5.6}$$

In the case of a fully-ionized atom, the IC channel is blocked due to the absence of bound electrons, thus the nucleus can only deexcite via photon emission. These two equations lead to:

$$\lambda_{IT}^{q=Z} = \frac{\lambda_{IT}^{q=0}}{\left(1 + \frac{\lambda_{IC}}{\lambda_\gamma}\right)}. \tag{5.7}$$

The ratio $\lambda_{IC}/\lambda_\gamma$ is equal to the ratio of the intensities of the corresponding processes I_{IC}/I_γ. This ratio of intensities is also known as *internal conversion coefficient*, and named α_{ICC}. The half-life of a fully-ionized isomeric state is determined from the α_{ICC} and the half-life of the neutral isomeric state as:

$$T_{1/2}^{q=Z} = T_{1/2}^{q=0}\left(1 + \alpha_{ICC}\right). \tag{5.8}$$

The known decay scheme of the 1348 keV isomeric state of ^{207}Tl and its half-life is presented in figure 5.2. The α_{ICC} given in literature [55] are respectively 0.146 for the main M4 transition to the 351 keV level, and 0.027 for the other E5 transition to the ground state. The calculated half-life for the fully-ionized isomeric state of $^{207}Tl^{81+}$ is:

$$T_{1/2}(theory) = 1.52(13)s. \tag{5.9}$$

This calculated value is in very good agreement with the experimental result of 1.47(32) s.

5.2 Isomeric production ratio of ^{207m}Tl

The isomeric production ratio R_{iso}, the ratio of the number of particles produced by the fragmentation process populating the isomeric state of $^{207}Tl^{81+}$ to all $^{207}Tl^{81+}$ particles produced by fragmentation, can be derived from the ratio of the frequency peak area of the isomeric state $N_m(t)$ to the areas sum of isomeric and ground states $N_m(t) + N_g(t)$ extrapolated to t = 0. The weighted average of the three runs is:

$$R_{iso}(experiment) = \frac{N_m(t=0)}{N_m(t=0) + N_g(t=0)} = 0.15(4). \qquad (5.10)$$

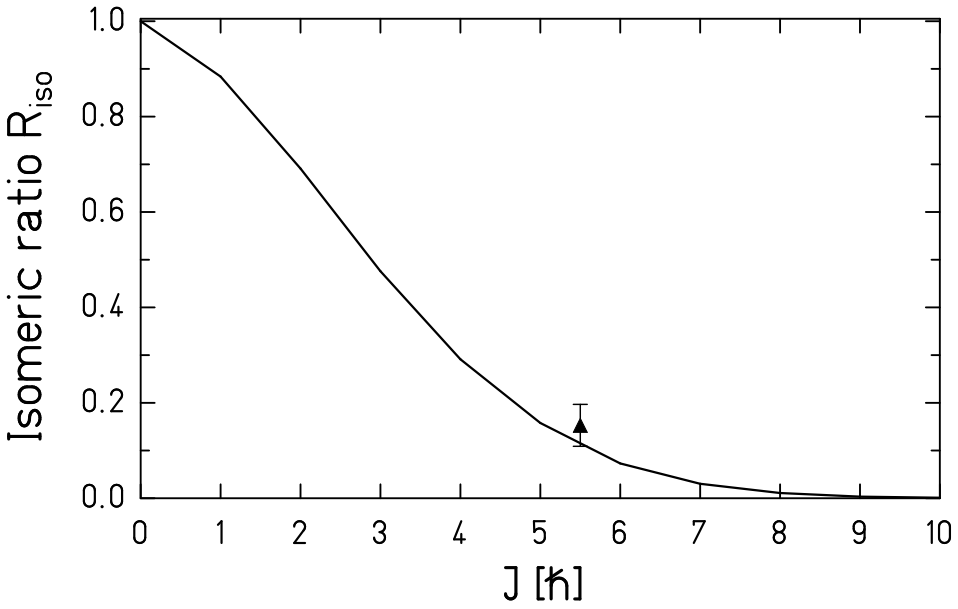

Figure 5.3: Comparison between the experimental isomeric production ratio (triangle) and calculations (solid line).

To derive the production probability of the isomeric state of $^{207}Tl^{81+}$ compared to all possible states, calculations [65] based on the abrasion-ablation model [66] were performed. The goal of the calculations is to determine the angular momentum distribution of the nuclides created by projectile fragmentation. This distribution depends strongly on the projectile energy, the mass numbers of both projectile A_p and fragment A_f, and the mass number difference between the two nuclides $\Delta A = A_p - A_f$. The maximum of the spin distribution will increase with increasing ΔA. On a first approximation the number of fragments going to a state with given spin is the integral of the distribution over the spin, going from 0 to the spin considered. It has to be normalized to the same integral, taking into account all possible spins, to give the fraction of particles going to a particular spin. An simplified analytic formula representing these calculations, taken from ref. [66], is shown in the following:

$$R_{iso} = \frac{\int_0^J (2J+1) e^{-\frac{J(J+1)}{2\sigma_n^2}} dJ}{\int_0^\infty (2J+1) e^{-\frac{J(J+1)}{2\sigma_n^2}} dJ}, \tag{5.11}$$

where J is the total spin of the nuclear state, σ_n a "spin-cutoff" parameter, depending of the mass numbers of the projectile A_p and fragment A_f involved in the fragmentation process, defined as:

$$\sigma_n^2 = 0.16 A_p^{2/3} \frac{(A_p - A_f)(\bar{\nu} A_p + A_f)}{(\bar{\nu}+1)^2 (A_p - 1)}, \tag{5.12}$$

where $\bar{\nu}$ is the mean number of evaporated nucleons per abraded mass unit. In the case of ^{207}Tl, as shown in figure 5.2, the spin of the isomeric state is 11/2, and $\Delta A = 1$. With such parameters the production probability of this isomeric state is expected to be rather small. The comparison between the calculations and the experimental result is presented in figure 5.3. The result obtained for spin 11/2 is:

$$R_{iso}(theory) = 0.11, \tag{5.13}$$

which is in excellent agreement with the value obtained in the experiment. Nevertheless more systematical studies of isomeric states production by projectile fragmentation have been performed [67], summarized in table 5.1, which show some discrepancies between calculations and experimental results. For small ΔA the calculation seem to underestimate the isomeric production ratio, whereas for higher ΔA the calculation overestimate this ratio.

Projectile	Fragment	ΔA	J^π	E^*(keV)	$T_{1/2}$ (s)	R_{iso}^{exp}	R_{iso}^{th}
^{209}Bi [9]	^{149}Dy	60	$27/2^-$	2661.1(4)	11(1)	0.23(2)	0.58
^{209}Bi [9]	^{151}Er	58	$27/2^-$	2585.5(6)	19(3)	0.21(3)	0.57
^{58}Ni [8]	^{52}Mn	6	2^+	377.749(5)	1380(180)	0.38(2)	0.65
^{58}Ni [8]	^{53}Fe	5	$19/2^-$	3040.4(3)	149(3)	0.10(1)	0.004
^{208}Pb	^{207}Tl	1	$11/2^+$	1348.1(3)	1.47(32)	0.15(4)	0.11

Table 5.1: Compilation for the different isomeric states evaluated in refs. [9], [8] and this work.

Appendix A

Results obtained from SONY data.

For each injection five parameters have been obtained from the fits, $N_{Tl}(0)$ and λ_{tot}^{Tl} using equation 3.10, $N_{Pb}(0)$, λ_b and λ_{loss} using equation 3.15. The decay constants listed are obtained in the *laboratory frame*. Also the ratio $N_{Pb}(0)/N_{Tl}(0)$ = R_{inj}, which represents the fraction of $^{207}Pb^{81+}$ contaminants injected in the ESR with the ions of interest $^{207}Tl^{81+}$, is given. The latter quantity is plotted in figure 2.5.

run #	$N_{Tl}(0)$	error	$N_{Pb}(0)$	error	$R_{inj}(\%)$	error
83	3323.95	54.28	60.64	4.91	1.82	0.15
84	2958.25	36.78	60.13	3.72	2.03	0.13
86	2196.66	31.67	41.13	3.16	1.87	0.15
87	1978.36	27.06	57.17	3.36	2.89	0.17
88	2360.61	37.54	43.93	3.51	1.86	0.15
90	3563.04	50.65	56.51	4.20	1.59	0.12
91	2519.84	47.10	24.41	3.96	0.97	0.16
92	2681.15	35.81	35.27	2.91	1.32	0.11
93	2611.89	31.69	34.65	2.65	1.33	0.10
94	2114.66	37.40	28.02	3.03	1.33	0.15
95	1552.54	25.35	21.19	2.18	1.36	0.14
96	1698.95	25.47	25.78	2.18	1.52	0.13
97	1714.01	26.01	14.60	2.12	0.85	0.12
98	1568.17	25.64	14.00	1.97	0.89	0.13
99	2156.80	33.04	26.00	2.89	1.21	0.14
100	1540.40	22.20	16.50	1.83	1.07	0.12
101	3146.65	52.81	28.32	4.00	0.90	0.13
102	3114.95	35.20	33.94	3.44	1.09	0.11
103	3642.15	54.26	39.54	4.29	1.09	0.12
104	2879.23	42.53	22.66	3.36	0.79	0.12
105	2999.87	55.33	33.70	4.18	1.12	0.14
106	2755.57	42.54	49.88	4.08	1.81	0.15
107	2698.25	43.05	8.53	2.97	0.32	0.11
108	5463.24	96.49	45.07	6.82	0.82	0.13

Table A.1: Summary of the results obtained from the SONY data for $N_{Tl}(0)$ and $N_{Pb}(0)$. R_{inj} is defined as the ratio $N^{Pb}(0)/N^{Tl}(0)$.

run #	$N_{Tl}(0)$	error	$N_{Pb}(0)$	error	$R_{inj}(\%)$	error
109	2988.45	54.76	34.66	3.85	1.16	0.13
110	4799.52	78.96	54.70	6.26	1.14	0.13
111	6541.03	109.56	108.59	10.06	1.66	0.16
113	3735.12	55.98	66.67	5.15	1.78	0.14
114	3227.70	52.86	47.88	4.62	1.48	0.15
116	4256.85	76.83	70.70	6.96	1.66	0.17
117	4581.33	58.70	61.97	5.36	1.35	0.12
118	4029.51	63.32	74.87	5.86	1.86	0.15
119	4988.85	80.07	81.53	6.99	1.63	0.14
120	4085.44	54.17	71.14	4.92	1.74	0.12
121	4424.42	65.13	74.67	5.84	1.69	0.13
122	5525.16	87.95	95.73	7.74	1.73	0.14
123	4537.62	55.41	71.36	4.76	1.57	0.11
124	3375.40	52.61	67.53	4.67	2.00	0.14
125	2335.74	36.25	43.69	3.53	1.87	0.15
126	3333.58	49.24	44.39	3.86	1.33	0.12
127	3301.48	47.19	60.54	4.46	1.83	0.14
128	2374.94	36.58	33.93	2.93	1.43	0.13
129	1469.45	19.69	33.36	2.08	2.27	0.14
130	1246.15	21.55	17.03	1.59	1.37	0.13
131	2880.89	48.97	57.82	4.55	2.01	0.16
132	3089.83	37.22	52.02	3.77	1.68	0.12
133	3551.84	52.11	54.93	4.73	1.55	0.14
135	2324.19	54.76	41.49	5.44	1.79	0.24

Table A.2: Summary of the results obtained from the SONY data for $N_{Tl}(0)$ and $N_{Pb}(0)$ (continued)

run #	λ_{tot}^{Tl}	error	λ_b	error	λ_{loss}	error
83	2.067E-3	1.510E-5	3.076E-4	9.871E-6	1.467E-4	2.486E-5
84	2.058E-3	1.154E-5	3.113E-4	7.955E-6	2.230E-4	1.948E-5
86	2.123E-3	1.343E-5	3.282E-4	9.466E-6	2.101E-4	2.217E-5
87	2.096E-3	1.298E-5	3.596E-4	1.080E-5	2.137E-4	2.176E-5
88	2.069E-3	1.487E-5	3.260E-4	9.858E-6	2.074E-4	2.389E-5
90	2.083E-3	1.501E-5	2.693E-4	8.194E-6	1.425E-4	2.693E-5
91	1.990E-3	1.729E-5	3.691E-4	1.139E-5	2.570E-4	2.816E-5
92	2.253E-3	1.264E-5	2.814E-4	7.331E-6	1.019E-4	1.973E-5
93	2.089E-3	1.140E-5	3.077E-4	6.913E-6	2.389E-4	1.864E-5
94	2.220E-3	1.645E-5	2.586E-4	9.394E-6	7.349E-5	2.629E-5
95	2.086E-3	1.522E-5	2.554E-4	8.801E-6	9.261E-5	2.516E-5
96	2.073E-3	1.414E-5	2.865E-4	8.368E-6	1.894E-4	2.310E-5
97	1.917E-3	1.404E-5	3.208E-4	8.390E-6	2.166E-4	2.366E-5
98	2.047E-3	1.555E-5	2.903E-4	8.458E-6	2.196E-4	2.448E-5
99	2.140E-3	1.428E-5	2.997E-4	8.818E-6	1.450E-4	2.301E-5
100	2.208E-3	1.371E-5	3.116E-4	8.132E-6	2.323E-4	2.179E-5
101	2.033E-3	1.544E-5	2.945E-4	8.808E-6	1.163E-4	2.501E-5
102	2.082E-3	1.066E-5	3.464E-4	7.318E-6	2.834E-4	1.800E-5
103	2.052E-3	1.369E-5	3.031E-4	8.089E-6	1.617E-4	2.245E-5
104	2.048E-3	1.371E-5	3.445E-4	8.435E-6	1.852E-4	2.177E-5
105	2.062E-3	1.127E-5	2.607E-4	6.664E-6	1.438E-4	8.772E-6
106	2.048E-3	1.256E-5	3.100E-4	6.397E-6	1.775E-4	6.479E-6
107	2.033E-3	1.476E-5	3.366E-4	8.232E-6	2.550E-4	2.324E-5
108	2.201E-3	1.678E-5	3.074E-4	9.378E-6	1.353E-4	2.695E-5

Table A.3: Summary of the results obtained from the SONY data for λ_{tot}^{Tl}, λ_b and λ_{loss}

run #	λ_{tot}^{Tl}	error	λ_b	error	λ_{loss}	error
109	2.034E-3	1.701E-5	2.891E-4	9.179E-6	2.280E-4	2.748E-5
110	2.052E-3	1.509E-5	3.280E-4	9.283E-6	2.222E-4	2.467E-5
111	2.148E-3	1.525E-5	3.339E-4	1.059E-5	2.009E-4	2.521E-5
113	2.003E-3	1.395E-5	3.116E-4	9.021E-6	2.498E-4	2.345E-5
114	2.053E-3	1.504E-5	3.236E-4	9.845E-6	1.821E-4	2.465E-5
116	2.116E-3	1.662E-5	3.365E-4	1.128E-5	2.575E-4	2.745E-5
117	2.146E-3	1.183E-5	3.126E-4	7.751E-6	1.467E-4	1.923E-5
118	2.060E-3	1.455E-5	3.099E-4	9.681E-6	1.807E-4	2.434E-5
119	2.170E-3	1.473E-5	2.893E-4	9.328E-6	7.920E-5	2.366E-5
120	2.108E-3	1.223E-5	3.074E-4	8.099E-6	2.153E-4	2.075E-5
121	2.030E-3	1.352E-5	3.225E-4	8.979E-6	1.624E-4	2.231E-5
122	2.130E-3	1.450E-5	3.012E-4	9.488E-6	1.707E-4	2.425E-5
123	2.103E-3	1.128E-5	2.873E-4	6.932E-6	1.599E-4	1.855E-5
124	1.968E-3	1.444E-5	2.857E-4	8.957E-6	1.698E-4	2.413E-5
125	2.052E-3	1.448E-5	3.056E-4	9.564E-6	1.981E-4	2.409E-5
126	2.101E-3	1.358E-5	2.911E-4	8.071E-6	1.549E-4	2.234E-5
127	2.015E-3	1.324E-5	3.341E-4	9.034E-6	2.225E-4	2.186E-5
128	1.913E-3	1.434E-5	2.922E-4	8.343E-6	2.057E-4	2.421E-5
129	2.094E-3	1.275E-5	2.356E-4	8.200E-6	1.036E-4	2.169E-5
130	2.220E-3	1.690E-5	2.580E-4	8.795E-6	6.230E-5	2.564E-5
131	2.056E-3	1.568E-5	2.711E-4	1.013E-5	1.007E-4	2.676E-5
132	2.052E-3	1.123E-5	3.432E-4	8.090E-6	2.727E-4	1.936E-5
133	2.034E-3	1.351E-5	3.466E-4	9.140E-6	2.522E-4	2.220E-5
135	2.091E-3	1.594E-5	2.750E-4	1.086E-5	1.680E-4	1.495E-5

Table A.4: Summary of the results obtained from the SONY data for λ_{tot}^{Tl}, λ_b and λ_{loss} (continued)

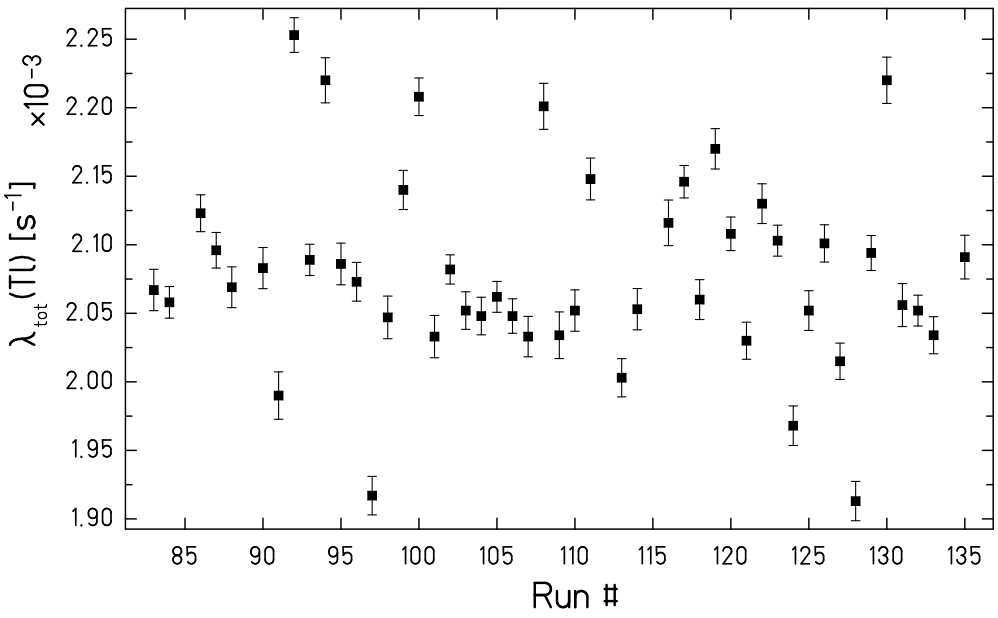

Figure A.1: Summary of λ_{tot}^{Tl} obtained for each run from the second experiment with SONY data.

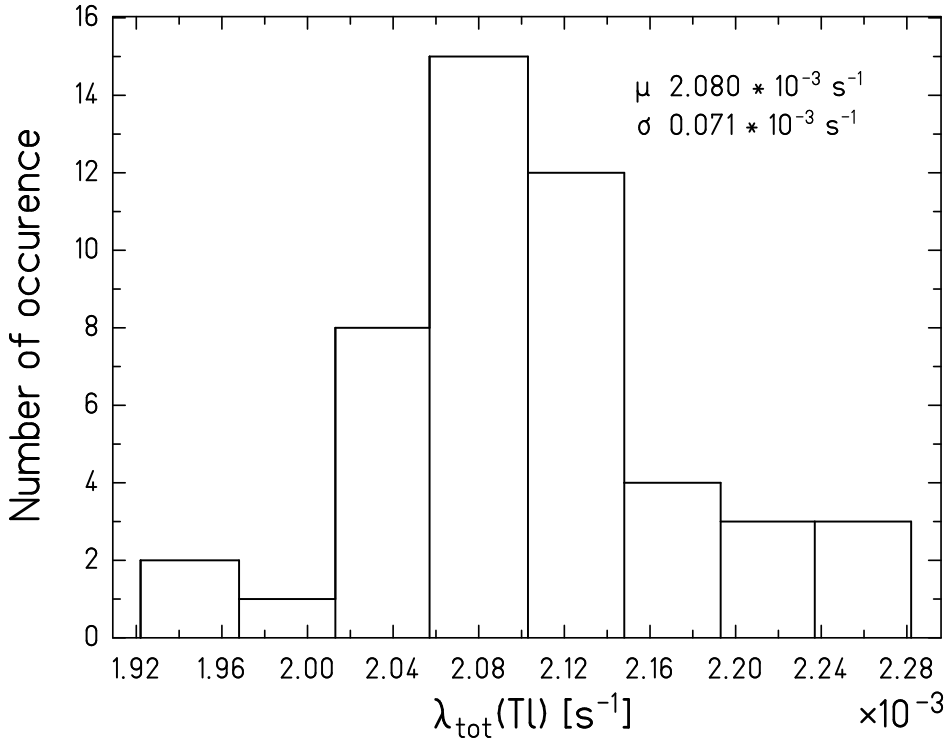

Figure A.2: Distribution of λ_{tot}^{Tl} from the second experiment with SONY data.

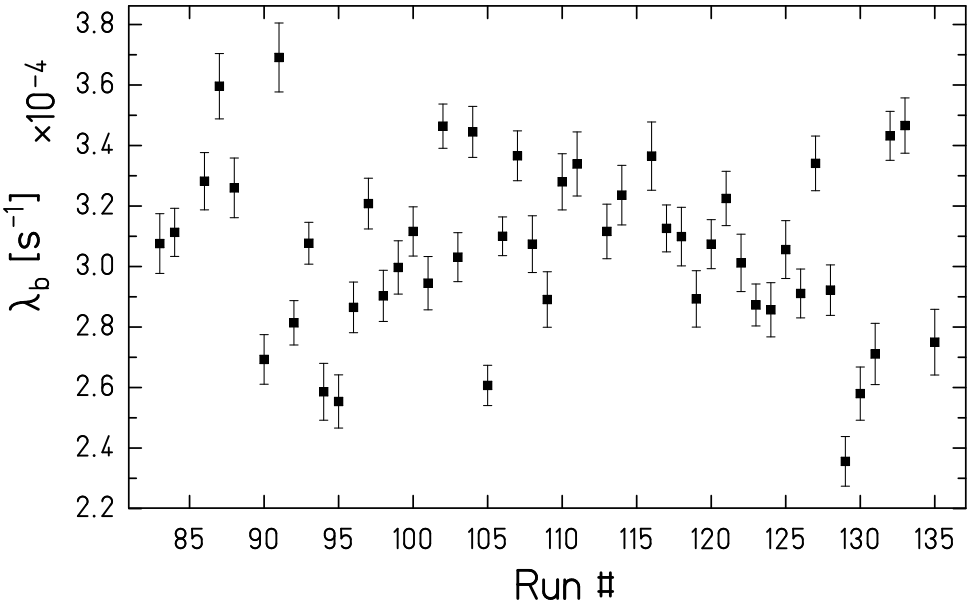

Figure A.3: Summary of λ_b obtained for each run from the second experiment with SONY data.

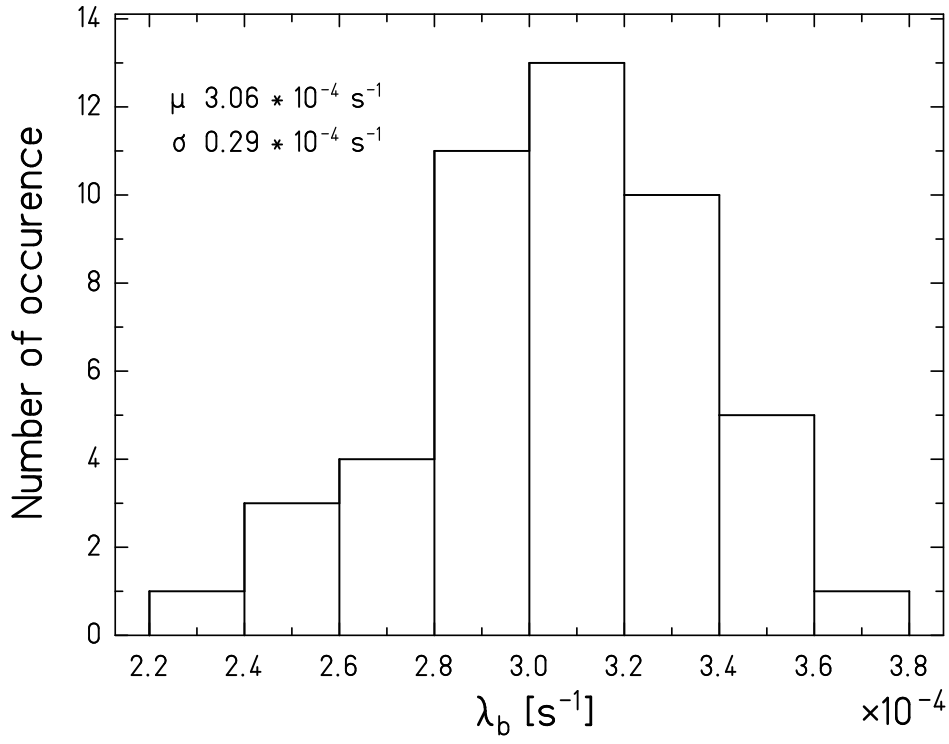

Figure A.4: Distribution of λ_b from the second experiment with SONY data.

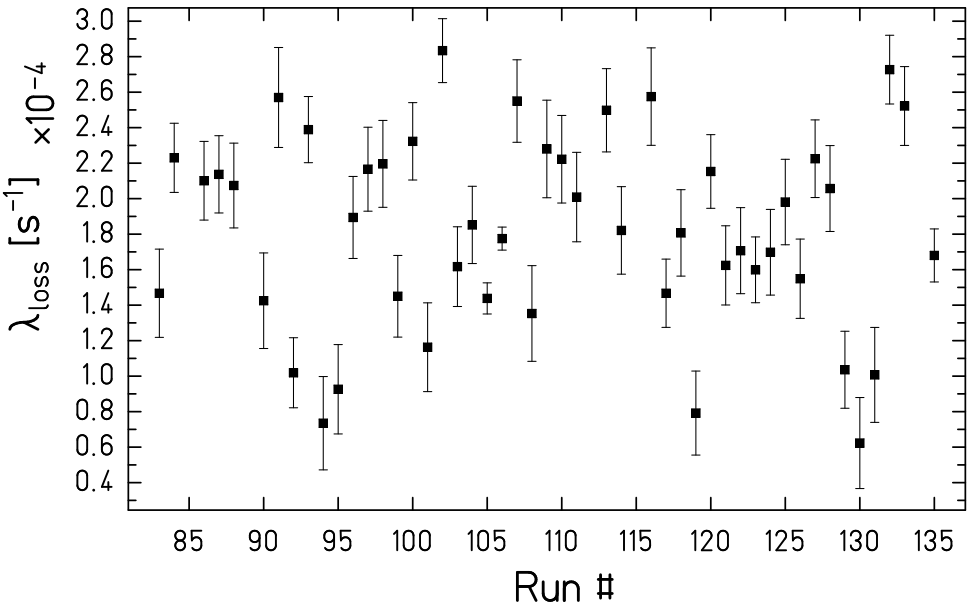

Figure A.5: Summary of λ_{loss} obtained for each run from the second experiment with SONY data.

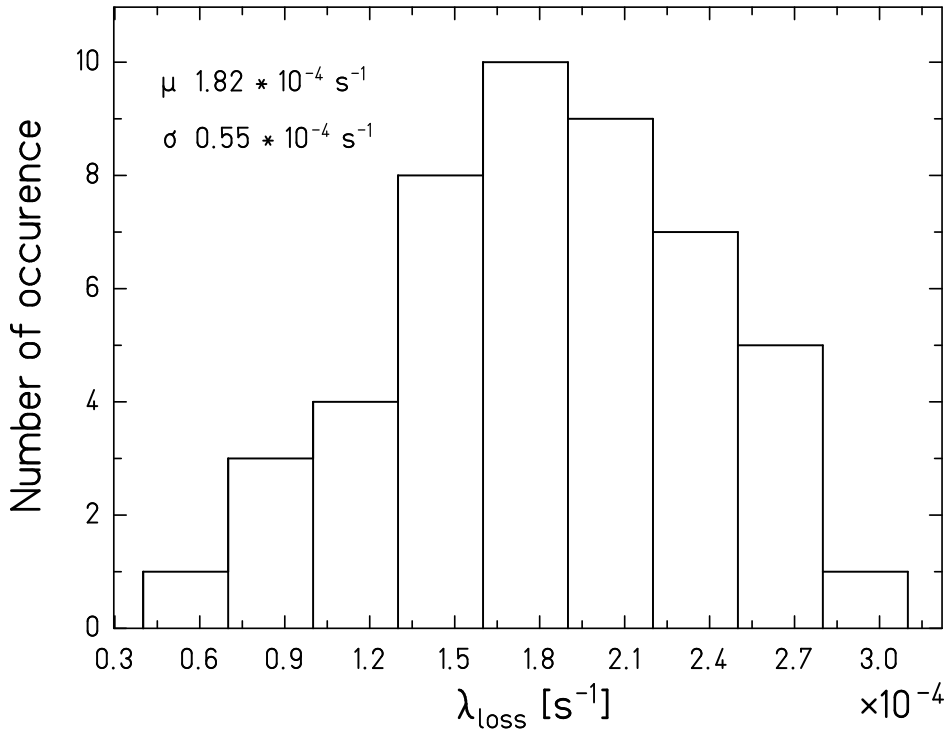

Figure A.6: Distribution of λ_{loss} from the second experiment with SONY data.

Appendix B

Results obtained from TCAP data.

For each injection five parameters have been obtained from the fits, $N_{Tl}(0)$ and λ_{tot}^{Tl} using equation 3.10, $N_{Pb}(0)$, λ_b and λ_{loss} using equation 3.15. The decay constants listed are obtained in the *laboratory frame*. Also the ratio $N_{Pb}(0)/N_{Tl}(0)$ = R_{inj}, which represents the fraction of $^{207}Pb^{81+}$ contaminants injected in the ESR with the ions of interest $^{207}Tl^{81+}$, is given. The latter quantity is plotted in figure 2.5.

run #	$N_{Tl}(0)$	error	$N_{Pb}(0)$	error	$R_{inj}(\%)$	error
83	3323.95	54.28	60.64	4.91	1.82	0.15
84	3127.64	48.53	68.69	5	2.20	0.16
86	2353.7	40.66	43.58	4.16	1.85	0.18
87	2076.45	28.56	56.69	3.55	2.73	0.18
88	2462.06	43.68	44.85	4.34	1.82	0.18
90	1559.3	25.38	19.09	1.73	1.22	0.11
91	2712.55	43.37	25.08	3.86	0.92	0.14
92	2912.78	38.82	35.81	3.33	1.23	0.12
93	2787.17	45.59	36.18	3.9	1.30	0.14
94	2313.26	40.72	20.18	5.08	0.87	0.22
95	1636.39	22.51	24.05	2.23	1.47	0.14
96	1767.78	27.05	27.29	2.66	1.54	0.15
97	1846.54	25.05	17.27	2.2	0.94	0.12
98	1657.02	32.31	15.37	2.66	0.93	0.16
99	2371.81	32.93	26.52	3.5	1.12	0.15
100	1659.65	26.21	19.56	1.99	1.18	0.12
101	3404.26	47.18	29.99	3.39	0.88	0.10
102	3375.42	59.96	42.07	5.53	1.25	0.17
103	3917.66	49.33	42.11	4.34	1.07	0.11
104	3091.44	54.82	21.27	3.99	0.69	0.13
107	2850.53	38.23	9.00	4.83	0.32	0.17
108	5757.69	56.51	42.92	7.73	0.75	0.13

Table B.1: Summary of the results obtained from the TCAP data for $N_{Tl}(0)$ and $N_{Pb}(0)$. R_{inj} is defined as the ratio $N^{Pb}(0)/N^{Tl}(0)$.

run #	$N_{Tl}(0)$	error	$N_{Pb}(0)$	error	$R_{inj}(\%)$	error
111	6648.98	63.63	141.19	13.37	2.12	0.20
113	3822.17	39.29	99.56	6.47	2.60	0.17
114	3454.43	39.49	63.08	6.34	1.83	0.18
115	5303.09	66.22	79.16	7.90	1.49	0.15
116	4481.27	45.48	80.80	8.35	1.80	0.19
117	5003.70	64.99	56.18	7.73	1.12	0.16
118	4359.75	37.91	102.62	6.79	2.35	0.16
119	5388.04	42.59	89.12	5.81	1.65	0.11
120	4305.05	41.15	79.09	10.13	1.84	0.24
121	4555.52	42.18	97.58	8.46	2.14	0.19
122	5942.36	76.82	111.64	9.92	1.88	0.17
123	4976.64	56.05	90.02	8.35	1.81	0.17
124	3660.22	46.29	83.30	5.67	2.28	0.16
125	2532.28	30.56	51.35	4.56	2.03	0.18
126	3753.53	46.59	44.70	5.19	1.19	0.14
127	3555.99	39.39	62.59	6.27	1.76	0.18
128	2561.45	33.80	36.55	4.56	1.43	0.18
129	1571.24	20.56	42.89	3.41	2.73	0.22
130	1342.17	17.39	24.92	2.72	1.86	0.20
131	3036.56	39.39	65.10	5.53	2.14	0.18
132	3353.17	43.75	65.06	6.06	1.94	0.18
133	3742.63	33.30	63.81	6.54	1.70	0.18

Table B.2: Summary of the results obtained from the TCAP data for $N_{Tl}(0)$ and $N_{Pb}(0)$ (continued)

run #	λ_{tot}^{Tl}	error	λ_b	error	λ_{loss}	error
84	2.052E-3	1.390e-5	3.067e-4	9.873E-6	2.178E-4	2.318E-5
86	2.139E-3	1.577E-5	3.403E-4	1.142E-5	2.665E-4	2.541E-5
87	2.095E-3	1.280E-5	3.646E-4	1.060E-5	2.052E-4	2.043E-5
88	2.048E-3	1.609E-5	3.398E-4	1.124E-5	2.478E-4	2.567E-5
90	2.119E-3	1.590E-5	2.640E-4	8.410E-6	1.160E-4	2.830E-5
91	1.996E-3	1.463E-5	3.645E-4	9.857E-6	2.403E-4	2.359E-5
92	2.266E-3	1.216E-5	2.875E-4	7.450E-6	1.256E-4	1.874E-5
93	2.076E-3	1.481E-5	3.005E-4	9.157E-6	2.117E-4	2.422E-5
94	2.227E-3	1.591E-5	2.771E-4	1.157E-5	1.257E-4	2.625E-5
95	2.088E-3	1.268E-5	2.583E-4	8.008E-6	1.011E-4	2.110E-5
96	2.038E-3	1.409E-5	2.949E-4	9.145E-6	1.960E-4	2.327E-5
97	1.931E-3	1.233E-5	3.113E-4	7.557E-6	1.959E-4	2.006E-5
98	2.021E-3	1.668E-5	2.931E-4	1.004E-5	2.124E-4	2.560E-5
99	2.171E-3	1.126E-5	2.966E-4	8.394E-6	1.481E-4	1.798E-5
100	2.227E-3	1.367E-5	3.074E-4	8.420E-6	2.282E-4	2.179E-5
101	2.053E-3	1.211E-5	2.975E-4	7.091E-6	1.235E-4	1.958E-5
102	2.103E-3	1.520E-5	3.342E-4	1.087E-5	2.624E-4	2.559E-5
103	2.055E-3	1.132E-5	3.041E-4	7.123E-6	1.755E-4	1.848E-5
104	2.048E-3	1.592E-5	3.398E-4	9.503E-6	1.740E-4	2.441E-5
107	2.008E-3	1.160E-5	3.290E-4	5.270E-6	2.450E-4	1.650E-5
108	2.187E-3	1.080E-5	3.100E-4	7.210E-6	1.470E-4	2.080E-5

Table B.3: Summary of the results obtained from the TCAP data for λ_{tot}^{Tl}, λ_b and λ_{loss}

run #	λ_{tot}^{Tl}	error	λ_b	error	λ_{loss}	error
111	2.083E-3	9.410E-6	3.340E-4	8.920E-6	2.000E-4	2.060E-5
113	1.950E-3	1.050E-5	2.990E-4	8.460E-6	2.010E-4	2.190E-5
114	2.045E-3	1.150E-5	3.180E-4	7.840E-6	1.700E-4	1.880E-5
115	2.112E-3	1.090E-5	3.350E-4	7.580E-6	2.100E-4	1.780E-5
116	2.091E-3	9.830E-6	3.440E-4	8.780E-6	2.650E-4	1.960E-5
117	2.156E-3	1.130E-5	3.180E-4	7.430E-6	1.660E-4	1.670E-5
118	2.042E-3	8.800E-6	2.990E-4	7.320E-6	1.620E-4	1.750E-5
119	2.178E-3	7.940E-6	2.890E-4	5.410E-6	6.030E-5	1.290E-5
120	2.079E-3	9.390E-6	3.260E-4	9.070E-6	2.380E-4	1.880E-5
121	1.983E-3	8.980E-6	3.340E-4	7.970E-6	1.620E-4	1.760E-5
122	2.120E-3	1.140E-5	3.030E-4	7.410E-6	1.500E-4	1.810E-5
123	2.112E-3	1.080E-5	2.900E-4	7.420E-6	1.560E-4	1.870E-5
124	1.965E-3	1.200E-5	3.020E-4	7.440E-6	2.240E-4	1.960E-5
125	2.033E-3	1.110E-5	3.040E-4	7.730E-6	2.120E-4	1.820E-5
126	2.113E-3	1.170E-5	2.920E-4	6.690E-6	1.820E-4	1.800E-5
127	2.002E-3	1.060E-5	3.540E-4	7.910E-6	2.590E-4	1.690E-5
128	1.904E-3	1.210E-5	3.170E-4	7.560E-6	2.640E-4	1.850E-5
129	2.069E-3	1.300E-5	2.390E-4	8.300E-6	9.350E-5	2.090E-5
130	2.211E-3	1.390E-5	2.500E-4	8.020E-6	4.950E-5	2.020E-5
131	2.037E-3	1.180E-5	2.940E-4	8.110E-6	1.240E-4	1.880E-5
132	2.060E-3	1.220E-5	3.390E-4	8.040E-6	2.610E-4	1.800E-5
133	1.997E-3	8.940E-6	3.510E-4	8.020E-6	2.520E-4	1.800E-5

Table B.4: Summary of the results obtained from the TCAP data for λ_{tot}^{Tl}, λ_b and λ_{loss} (continued)

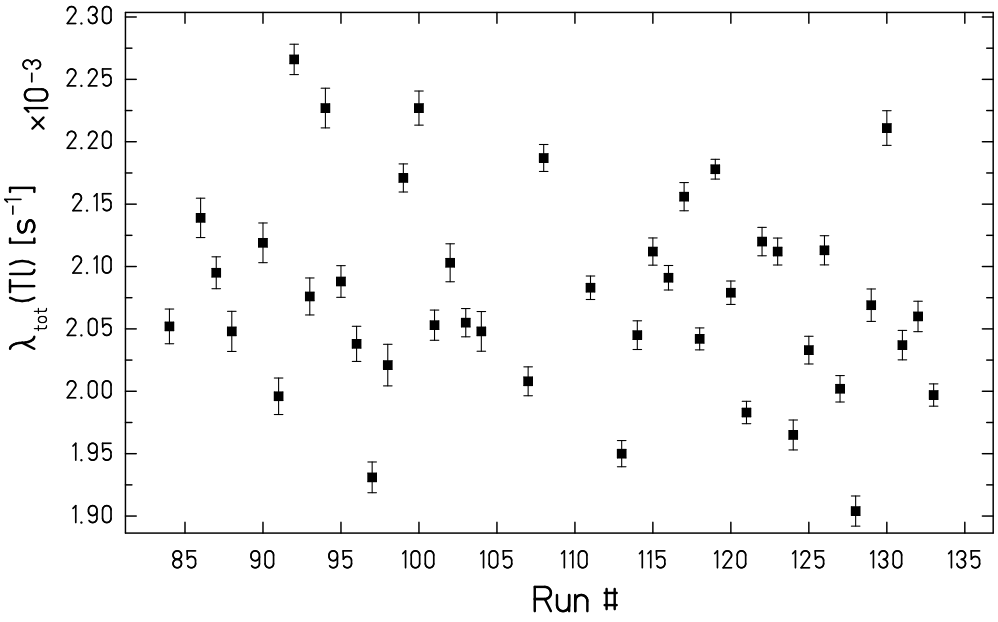

Figure B.1: Summary of λ_{tot}^{Tl} obtained for each run from the second experiment with TCAP data.

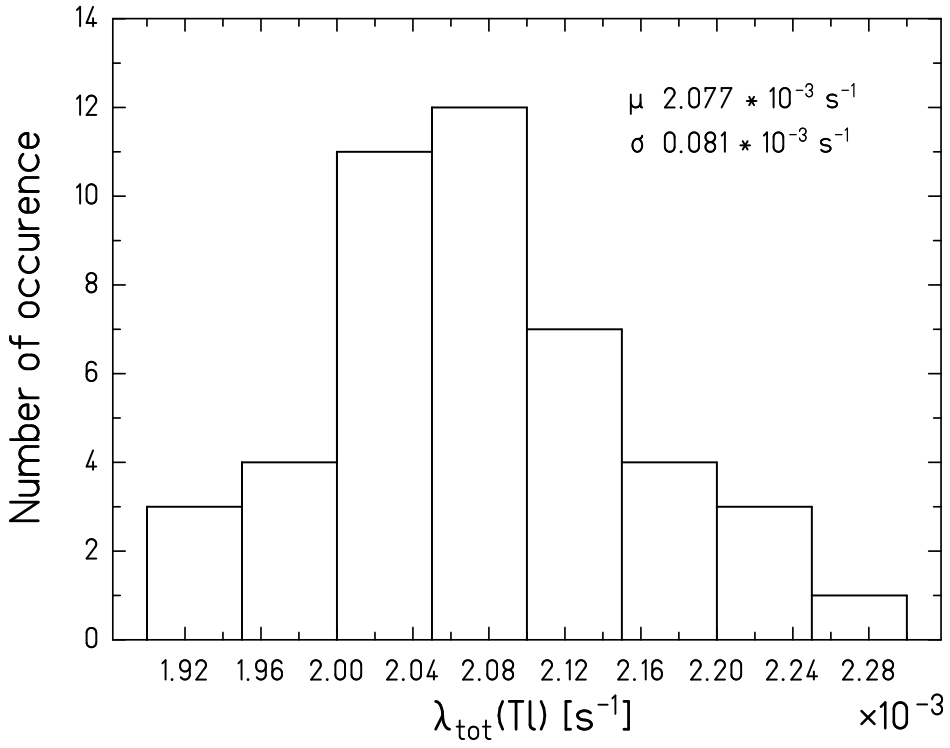

Figure B.2: Distribution of λ_{tot}^{Tl} from the second experiment with TCAP data.

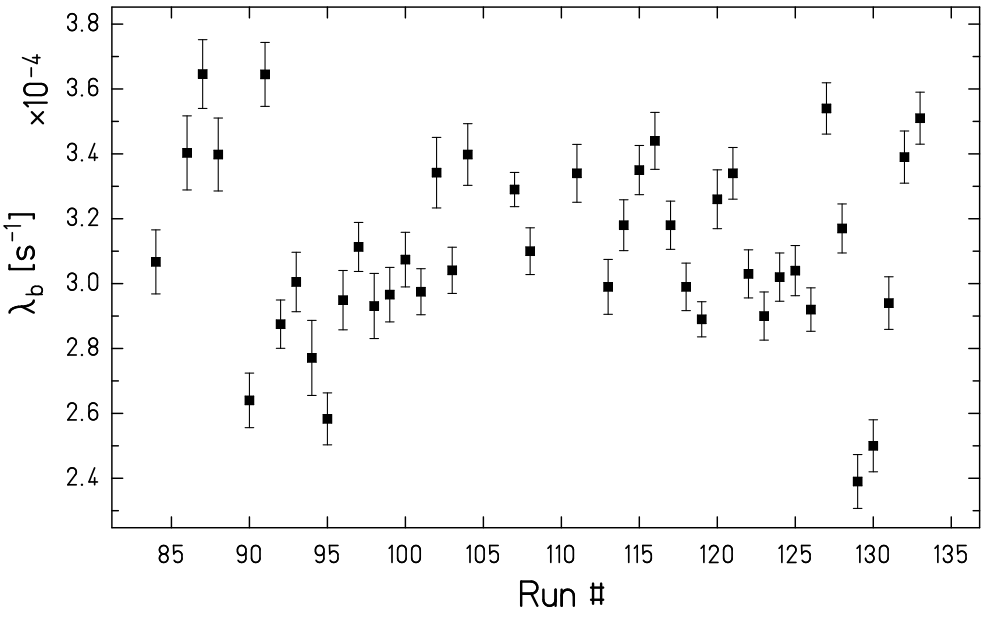

Figure B.3: Summary of λ_b obtained for each run from the second experiment with TCAP data.

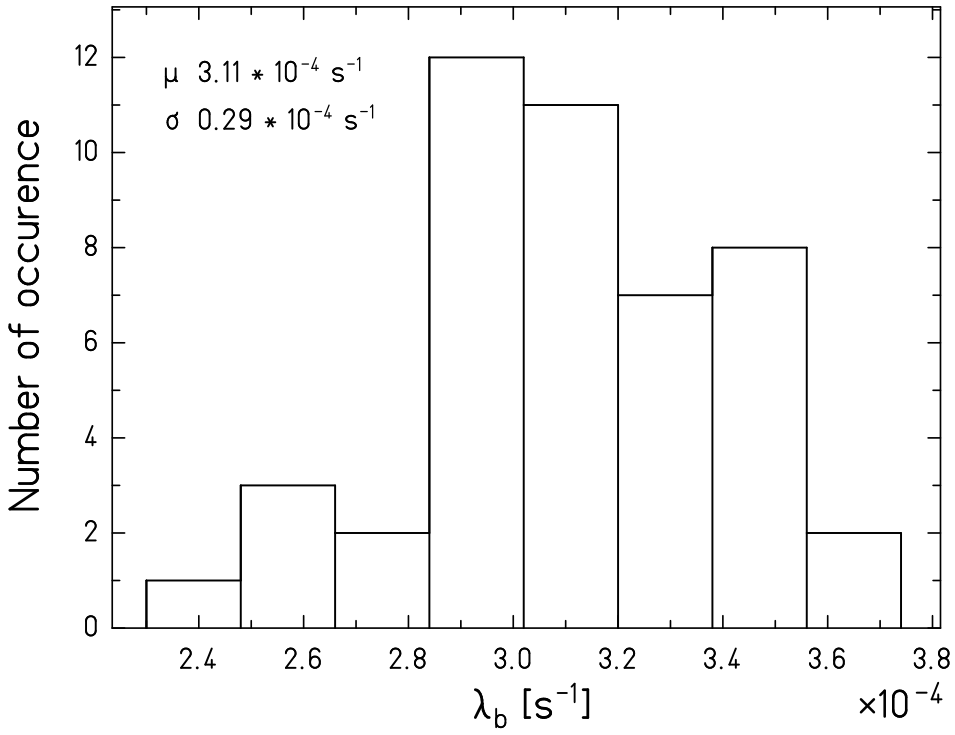

Figure B.4: Distribution of λ_b from the second experiment with TCAP data.

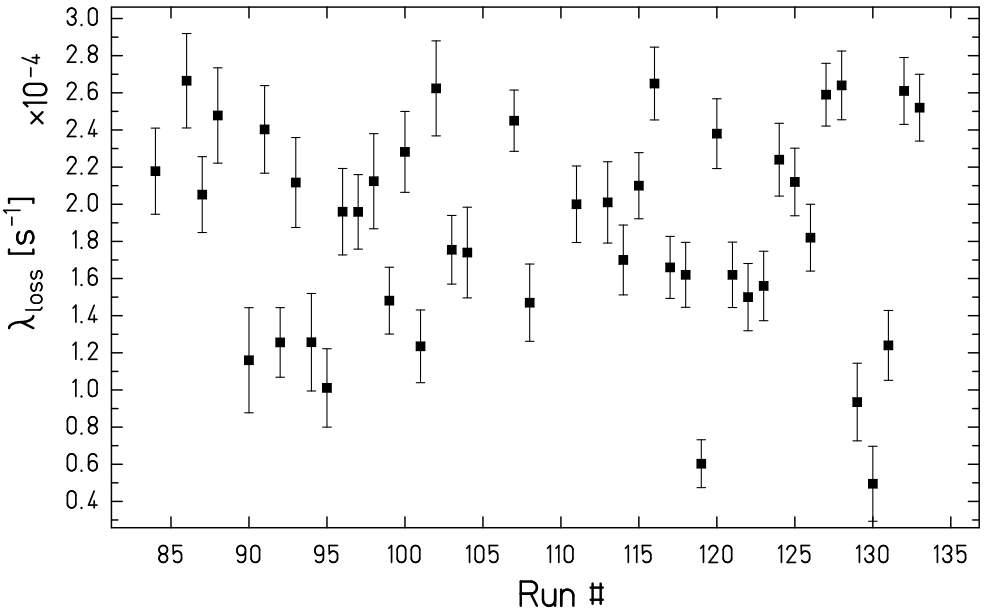

Figure B.5: Summary of λ_{loss} obtained for each run from the second experiment with TCAP data.

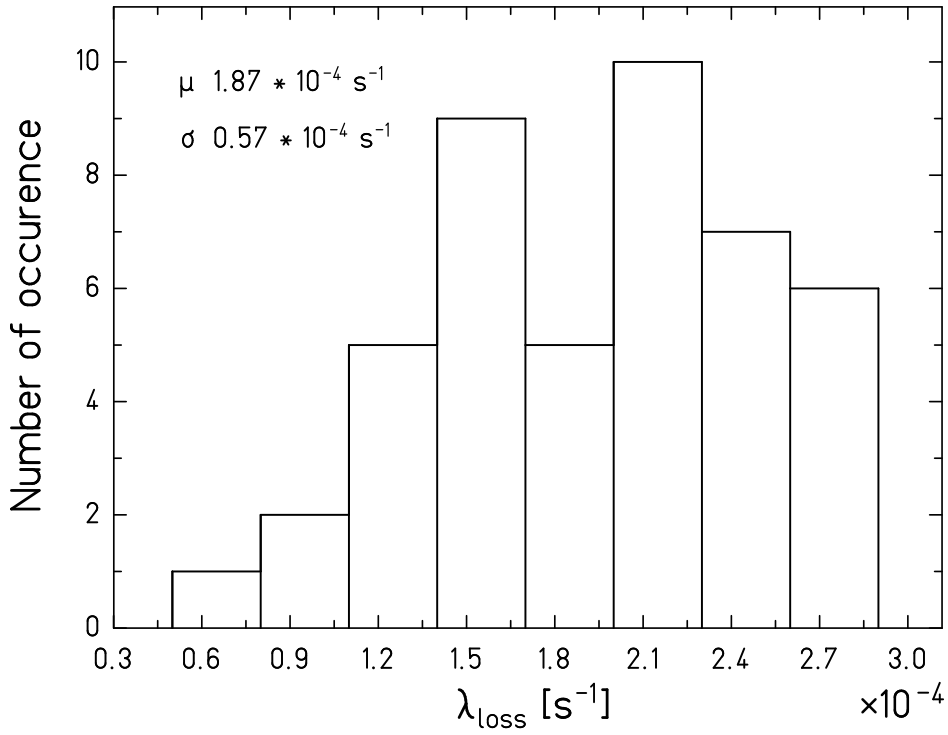

Figure B.6: Distribution of λ_{loss} from the second experiment with TCAP data.

Bibliography

[1] M. Curie, O. Kammerlingh, Le Radium **10** (1913) 181.

[2] K. W. F. Kohlrausch, *Radioaktivivät*, Handbuch der Experimentalphysik, **15**, Leipzig, Akad. Verlagsgesellschaft (1928).

[3] G. T. Emery, Ann. Rev. Nucl. Sc. **22** (1972) 165.

[4] See Nucl. Data Sheets series or http://www.nndc.bnl.gov/ensdf/index.jsp.

[5] F. Bosch, Phys. Scr. **T59** (1995) 221.

[6] V. A. Erma, Phys Rev. **105** (1957) 1784.

[7] A. Musumarra, nucl-th/0412036.

[8] H. Irnich *et al.*, Phys Rev. Lett. **75** (1995) 4182.

[9] Yu. A. Litvinov *et al.*, Phys. Lett. **B573** (2003) 80.

[10] R. Daudel *et al.*, J. de Physique et de Radium **8** (1947) 238.

[11] J. Chadwick, Verh. D. Phys. Ges. **16** (1914) 383.

[12] C. L. Cowan, Science **124** (1956) 103.

[13] E. Fermi, Z. Phys., **88** (1934) 161.

[14] T. D. Lee, C. N. Yang, Phys. Rev. **104** (1956) 254.

[15] C. S. Wu *et al.*, Phys. Rev. **105** (1957) 1413.

[16] H. V. Klapdor-Kleingrothaus *et al.*, Mod. Phys. Lett. **16** (2001) 2409.

[17] F. W. Aston, Proc. of the Royal Society **A115** (1927) 487.

[18] B. Povh *et al.*, *Particles and Nuclei: An Introduction to the Physical Concepts*, Second Edition, Springer, 1999.

[19] Ch. Weinheimer *et al.*, Phys. Lett. **B460** (1999) 219.

[20] Y. Fukuda *et al.*, Phys. Rev. Lett. **81** (1998) 1562.

[21] C. Scheidenberger *et al.*, AIP Conf. Proc. **512** (2000) 275.

[22] J. N. Bahcall, Phys Rev. **124** (1961) 495.

[23] K. Takahashi, K. Yokoi, At. Data Nucl. Data Tables **36** (1987) 375.

[24] W. Bambynek *et al.*, Rev. Mod. Phys. **49** (1977) 77.

[25] J. P. Desclaux, At. Data. Nucl. Data Tables **12** (1973) 311.

[26] W. R. Johnson and G. Soff, At. Data. Nucl. Data Tables **33** (1985) 405.

[27] G. Audi *et al.*, Nucl. Phys. **A729** (2003) 3;
G. Audi *et al.*, Nucl. Phys. **A729** (2003) 337.

[28] E. M. Burbidge *et al.*, Rev. Mod. Phys. **29** (1957) 547.

[29] P. W. Merrill, Science **115** (1952) 484.

[30] F. Käppeler *et al.*, Ann. Rev. Nucl. Part. Sci. **48** (1998) 175.

[31] F. Käppeler *et al.*, Prog. Part. Nucl. Phys. **43** (1999) 419.

[32] M. Jung *et al.*, Phys. Rev. Lett. **69** (1992) 2164;
M. Jung, *Erste Messung des Betazerfalls in Gebundene Zustände des Elektrons:* $^{163}_{66}Dy^{66+} \rightarrow ^{163}_{66}Ho^{66+} + \bar{\nu}_e$, PhD Thesis, Technische Universät München, 1994.

[33] K. Takahashi, K. Yokoi, Nucl. Phys. **A404** (1983) 578.

[34] S. Yasumi *et al.*, Phys. Lett. **B181** (1986) 169.

[35] E. Laegsgaard *et al.*, in *Proceedings of the Seventh International Conference on Atomic Masses and Fundamental Constants (AMCO-7), Darmstadt-Seeheim, 1984*, edited by O. Klepper (1984) 652.

[36] D. D. Clayton, Nature **224** (1969) 56.

[37] K. Yokoi *et al.*, Astron. Astroph. **117** (1983) 65.

[38] R. B. Firestone, Nucl. Data Sheets **62** (1991) 159.

[39] K. Takahashi *et al.*, Phys. Rev. **C36** (1987) 1522.

[40] M. Galeazzi *et al.*, Phys. Rev. **C63** (2001) 014302.

[41] F. Bosch *et al.*, Phys Rev. Lett. **77** (1996) 5190.

[42] B. Franzke *et al.*, Phys. Scr. **T59** (1995) 176.

[43] H. Geissel *et al.*, Ann. Rev. Part. Nucl. Sci. **45** (1995) 163.

[44] S. Hofmann, G. Münzenberg, Rev. Mod. Phys. **72** (2000) 733.

[45] H. Geissel *et al.*, Nucl. Instr. and Meth. in Phys. Res. **B204** (2003) 71.

[46] H. Geissel *et al.*, Nucl. Instr. and Meth. in Phys. Res. **B70** (1992) 286.

[47] H. Bethe *et al.*, Z. Phys. **76** (1932) 293.

[48] C. Scheidenberger, H. Geissel, Nucl. Instr. Meth. **B135** (1998) 25.

[49] B.Franzke *et al.*, Nucl. Instr. Meth. **B24/25** (1987) 18.

[50] M. Steck *et al.*, AIP Conf. Proc. **457** (1999) 87.

[51] M. Steck *et al.*, Nucl. Instr. Meth. **A532** (2004) 357.

[52] R. W. Hasse, Phys. Rev. Lett. **90** (2003) 204801.

[53] J. N. Trischuk and E.Kankeleit, Nucl. Phys. **A90** (1967) 33.

[54] H. Behrens, J. Jänecke, *Numerical Tables for Beta-Decay and Electron-Capture*, Springer-Verlag, 1969.

[55] M. J. Martin, Nucl. Data Sheets **70** (1993) 315.

[56] SONY TEKTRONIX 3066 & 3086 3 GHz Real Time Spectrum Analyzer User Manual.

[57] T. Ohtsubo *et al.*, to be published.

[58] F. Nolden, Nucl. Instr. Meth. **A441** (2000) 219.

[59] Yu. A. Litvinov, *Basic Nuclear Properties of Neutron-Deficient Nuclei Investigated via High Precision Mass Measurements in the Element Range of* $36 \leq Z \leq 92$, PhD Thesis, Justus-Liebig Universät Giessen, 2004.

[60] E. Kaza, *First Mass Measurements of Stored and Cooled Neutron-rich* ^{238}U *Projectile Fragments in the Element Range of* $87 \leq Z \leq 92$ *at the FRS-ESR Facility*, PhD Thesis, Justus-Liebig Universät Giessen, 2004.

[61] B. Schlitt, *Schottky Mass Spectrometry at the Heavy Ion Storage Ring ESR*, PhD Thesis, Universät Heidelberg, 1997.

[62] T. Radon *et al.*, Nucl. Phys. **A677** (2000) 75.

[63] http://www-w2k.gsi.de/charms/SATAN/graf.htm.

[64] D. Eccleshall, M. J. L. Yates, Phys. Lett. **19** (1965) 301.

[65] K.-H. Schmidt, A. Kelic, private communication.

[66] M. de Jong *et al.*, Nucl. Phys. **A613** (1997) 435.

[67] D. Boutin *et al.*, GSI Report 2005, in print.

Acknowledgments

I would like to thank all the people that helped me to make all this possible. First, I thank Dr. Christoph Scheidenberger to have introduced me to the research in Physics, already 5 years ago. I am grateful to Prof. Dr. Gottfried Münzenberg to have allowed me to work at GSI for my PhD work. I am thankful to Prof. Dr. Hans Geissel to have supervised my work during my stay in GSI, and to Prof. Dr. Fritz Bosch for fruitful discussions and being always attentive to my problems and questions.
I am grateful to all the past and present members of our group, Prof. Dr. Yuri N. Novikov, Dr. Evangelia Kaza, Dr. Milan Matos, Dr. Takayuki Yamaguchi, Dr. Yuri A. Litvinov, Dr. Gleb Vorobjev, Serguei Litvinov, Ronia Kñobel and others for all they have contributed to my work.
I want to thank all the colleagues for the nice atmosphere that they put in my office, Dr. Leonid Grigorenko, Dr. Mauricio Portillo and especially Dr. M. Maier (never change a winning team!).
Special thanks go to all the members of the "company" that I had the chance to meet during all this time. They are too numerous to name all of them, but I will not forget in particular Dr. Alexandre Gumberidze, Dr. Markus Kirk, Dr. Anton Andronic, and least but not least, Georgios Tsiledakis.
And finally I would like to thank all my family, my parents and my brothers, for all their support during this period, despite being far from the eyes, they are close from the heart.